Convective initiation on 19 June 2002 during IHOP: High-resolution simulations and analysis of the mesoscale structures and convection initiation

Qi-Wei Wang[1,2] and Ming Xue[2,3]

Received 31 January 2012; revised 24 April 2012; accepted 9 May 2012; published 27 June 2012.

[1] The 19 June 2002 convective initiation (CI) case from the International H_2O Project (IHOP) is simulated using the ARPS at 1 km grid spacing. It involves three distinct CI groups, CI-A, CI-B, and CI-C, associated with a cold front-dryline system. Initial condition at 1800 UTC, 19 June 2002 was created using the ARPS 3DVAR, including standard as well as special observations. The simulation captured the three groups of CIs rather well, with small timing and spatial errors. CI-A is most typical of dryline initiation. Vertical cross sections through the initiation locations show typical dryline structures with an upward moisture bulge forced by lifting along the dryline convergence. For CI-B, the model-predicted mesoscale structures agree with special IHOP aircraft dropsonde observations closely. Strong low-level convergence from opposing cold front and dryline circulations produces deep symmetric upwelling of moist air, and the convection is initiated at the crest of the moisture bulge. CI-C is more typical of frontal convection where deep convection is first initiated at the front edge of the cold air. For CI-B and CI-C, north-south moisture bands that have dryline characteristics (and can be considered multiple drylines) and contain enhanced vertical motion and upward moisture bulges intercept the dryline and cold front, respectively, providing the most favored locations on the dryline or cold front for initiation. Furthermore, the air parcels feeding the initial cells at CI-B and CI-C have trajectories along the moisture bands and have already experienced uplifting when they reach the dryline and cold front locations.

Citation: Wang, Q.-W., and M. Xue (2012), Convective initiation on 19 June 2002 during IHOP: High-resolution simulations and analysis of the mesoscale structures and convection initiation, *J. Geophys. Res.*, *117*, D12107, doi:10.1029/2012JD017552.

1. Introduction

[2] Accurate prediction of warm-season convective rainfall continues to be a challenge [*Fritsch and Carbone*, 2004]. To improve quantitative precipitation forecasting (QPF) skills, it is important to improve our knowledge and understanding on the timing, location and processes of convective initiation (hereafter, CI) [*Weckwerth and Parsons*, 2006; *Weckwerth et al.*, 2004]. While the prediction of CI is directly related to the representation of small-scale physical processes in numerical weather prediction (NWP) models, it is also highly dependent on the mesoscale environment, in particular, the temperature, moisture and wind conditions within the planetary boundary layer (PBL) [*Crook*, 1996; *Weckwerth et al.*, 1996]. To help understand the CI processes and improve QPF, the International H_2O Project (IHOP_2002 or IHOP) [*Weckwerth et al.*, 2004] field experiment was carried out in the spring of 2002 over the Central Great Plains of the United States.

[3] *Wilson and Roberts* [2006] summarized the major CI events and their evolution during the IHOP_2002 period based on observational data; significant CI cases on 24 May, June 12, and June 19, 2002 were highlighted in their paper. *Xue and Martin* [2006a, 2006b, hereinafter XM06a and XM06b] numerically simulated the May 24 case using the Advanced Regional Prediction System (ARPS) [*Xue et al.*, 2000, 2003, 2001] and obtained rather accurate simulation of the initiation of three initial convective cells along the dryline. A conceptual model was proposed in XM06b that emphasizes the interaction of the fine-scale boundary layer horizontal convective rolls (HCRs) with the mesoscale convergence zone along the dryline for determining the exact CI locations. Using a similar approach, *Liu and Xue* [2008, hereinafter LX08] successfully simulated the CI events and subsequent storm evolutions in the 12 June 2002 case. That case also involved a dryline and a cold front, plus an outflow boundary left behind by an earlier mesoscale

[1]Key Laboratory of Mesoscale Severe Weather and School of Atmospheric Sciences, Nanjing University, Nanjing, China.
[2]Center for Analysis and Prediction of Storms, University of Oklahoma, Norman, Oklahoma, USA.
[3]School of Meteorology, University of Oklahoma, Norman, Oklahoma, USA.

Corresponding author: M. Xue, Center for Analysis and Prediction of Storms, University of Oklahoma, 120 David L. Boren Blvd., Norman, OK 73072, USA. (mxue@ou.edu)

0148-0227/12/2012JD017552

convective system. The outflow boundary intercepted both cold front and dryline near its west end. The simulations captured rather well the initiation of several groups of convective cells along the dryline and/or ahead of the outflow boundary, as well as a later secondary initiation along a new outflow boundary.

[4] Even with the commonly recognized focusing role of the dryline-cold front "triple point" on May 24 and June 12, forecasting the precise timings and locations of CIs for field deployment of mobile observing platforms had proven to be quite a challenge; in fact, on both days most observing platforms missed the primary CI regions [*Markowski et al.*, 2006; *Wilson and Roberts*, 2006]. A more successful deployment was carried out on the third IHOP CI case of June 19, 2002 [*Wilson and Roberts*, 2006]. This case also involved intersecting dryline and cold front, but was more complex involving three distinct CIs, along a dryline to the south, near a dryline-cold front triple point in the middle, and at a cold front to the north. Field data collections were focused on the second region of CI.

[5] The evolution and structure of the dryline and associated CI on June 19 had been studied in several observation-based papers [*Marquis et al.*, 2007; *Miao and Geerts*, 2007; *Murphey et al.*, 2006; *Sipprell and Geerts*, 2007; *Wakimoto and Murphey*, 2010]. *Murphey et al.* [2006, M06 hereinafter] documented the vertical structure across the dryline based on a series of dropsondes deployed from an aircraft; the prominent feature over the dryline was a strong upward moisture bulge above which convection initiation occurred. They suggested that such a bulge and associated initiation of convection resulted from the diurnally induced easterly flow in the maritime air east of the dryline that developed late in the day; this flow increased the low-level convergence and allowed rising parcels of air to reach the level of free convection.

[6] Detailed convection-resolving modeling study with focus on the CI process has not been performed on the June 19 case, according to the authors' knowledge. *Jankov et al.* [2007] investigated the sensitivity of precipitation forecast skills to physics parameterizations and two types of initial conditions using the WRF-ARW model with a 12 km grid spacing, for eight cases including that of June 19. *Trier et al.* [2008] studied the sensitivity of PBL and precipitation forecasting (with 4 km grid spacing) to land surface model and soil wetness conditions during a 12-day period covering the June 19th. None of those studies focused specifically on this particular case or the CI issue.

[7] The purposes of this study are twofold: the first is to obtain an as realistic as possible high-resolution simulation of this case by assimilating additional high-resolution observations, and establishes the credibility of the simulation of the mesoscale evolutions of dryline and cold fronts and associated CIs through verifications against available observations, and the second is to document the mesoscale features at and near the dryline and cold fronts and to understand their roles in the CIs through diagnostic analyses and additional simulation experiments. The fact that several CIs occurred at different parts of the dryline-cold front system on that day that may have been subjected to different mesoscale environment and forcing makes this case particular interesting, while the complexity of this case also poses extra challenges to the numerical model. According to our knowledge, attempts made by some other groups with this case have met with less success. Our simulation results will be discussed in the context of existing observational studies, especially those of M06, for the second CI region. The first and third CI regions had not been studied in published papers, as far as we know.

[8] The rest of this paper is organized as follows. In section 2, we discuss the synoptic and mesoscale environment of the 19 June 2002 case, the cold front-dryline system, and the observed initiation and evolution of convective cells of interest. Section 3 introduces the numerical experiments. The observational data sets, data analysis method and procedure, and the numerical model used and its configurations are described. The general evolutions of the predicted CI groups on the 1 km grid are first compared with radar observations in section 4 to establish the credibility of the model predictions. Section 5 presents a detailed analysis of the predicted mesoscale features at and around the CI locations and discusses the causes and effects of these mesoscale features in relation to the three CI groups. Section 6 presents a summary and conclusions.

2. Overview of the 19 June 2002 Case

[9] At 1800 UTC (hereafter, all times are UTC) 19 June 2002, moderately strong southerly flows are found over western Kansas at the 250-hPa level associated with a shortwave trough to its west and an anticyclone circulation to its east (Figure 1a). At the 500-hPa level (Figure 1b), relatively strong southwesterly winds between the trough and anticyclone can be seen crossing Kansas-Colorado border. Western Kansas is located ahead of the upper-level shortwave trough, providing a generally favorable condition for deep convection. Surrounding the trough at the 700 hPa level are three air masses (Figure 1c); the cold northwesterly air mass west and the moist south-southwesterly air mass east of the trough line, and the westerly plateau air mass to the south and southwest. At the 850 hPa level, the tough line is a boundary clearly dividing northerly and south-southwesterly flows (Figure 1d) while the dry plateau air is located above this level (therefore invisible here). This trough line matches the surface cold front found in Figure 2.

[10] At the surface, a low pressure was centered in central South Dakota (Figure 2a). The surface cold front extended south from this center. Behind the cold front was shallow cold air that moved along the eastern flank of Colorado Rocky Mountains, advancing the cold front southeastward toward the dryline (Figure 2a). A secondary cold front was located behind the cold front over the Colorado-Nebraska border. At 1800 UTC near Colorado-Kansas border, the surface cold front was less than 100 km behind the dryline (Figure 2), and a cold front-dryline triple point was located near the northwestern corner of Kansas (Figure 2a). As the cold front advanced and was catching up with the dryline, the triple point shifted southward along the dryline (see later Figure 9). In the process, dry air was sandwiched between the dryline and advancing cold front.

[11] Figure 2b shows the convective available potential energy (CAPE) and convective inhibition (CIN) maps at 1800. Large-CAPE regions are seen near and to the east of the cold front and dryline. A local CAPE maximum (denoted by H1) of over 3500 J kg^{-1} is found ahead of the cold front in southwest Nebraska, where there is less CIN. This CAPE

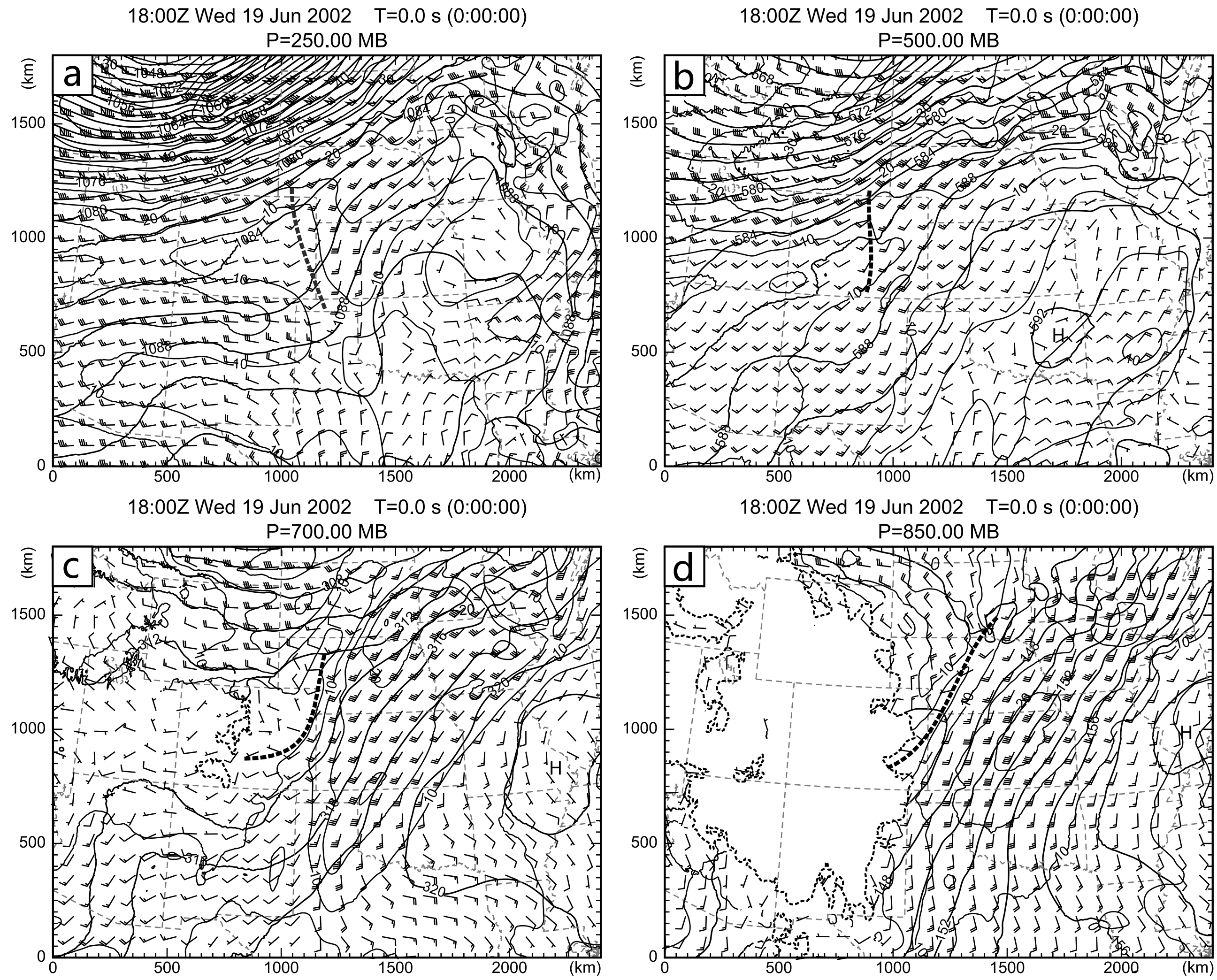

Figure 1. Geopotential height (thick black contours, 10 m), wind speed (thin black contours, m s^{-1}), and wind barbs (one full bard = 5 ms^{-1}) at 1800 UTC 19 June 2002, at (a) 250-, (b) 500-, (c) 700-, and (d) 850 hPa levels. Bold dashed lines indicate the locations of trough lines. The thin dashed lines in Figures 1c and 1d indicate where the pressure level intersects the ground. These fields are plotted from 1800 UTC Eta analysis.

maximum is linked to the third CI of this case. Another CAPE maximum is found east of the dryline over Oklahoma panhandle (denoted by H2) which may be linked to the first CI. Between the two maxima is a transition zone of considerable CAPE and moderate CIN, while a region of larger CIN (denoted by ***H***) is found further to the east.

[12] Figure 3 shows the GOES visible images taken at 1945, 2015, 2045, 2115, 2145 and 2215 on 19 June 2002. At 1945, the cold front and dryline can be analyzed with the aid of observed clouds (Figure 3a). A segment of clouds found over southeastern Colorado at this time (as indicated by the white arrows in Figure 3a) developed into a cumulus cloud (denoted A in Figure 3b, hereafter, CI-A) by 2015 (Figure 3b). This cloud is also seen in radar observations at 2000 (see later Figure 5a), although the precipitation echo was still rather weak at that time.

[13] By 2045 (Figure 3c), CI-A had further developed, and at the same time, a line of small cells appeared over northwestern Kansas (denoted convection line in Figure 3), northeast of CI-A. At 2115 (Figure 3d), CI-A became further developed, and its clouds became connected with this line of cells. From 2115 to 2145 UTC, two new convective clouds (denoted B and C in Figure 3, hereafter, CI-B and CI-C) formed quickly as shown in Figure 3d and Figure 3e. By 2215 (Figure 3f), the anvils of all three cell groups become almost connected; at this time, CI-A started to weaken while CI-B and CI-C were exhibiting strong growth. All three cell groups can be seen in the radar reflectivity observations at 2200 (see later Figure 5c), with CI-B being the weakest at this time. These satellite and radar observations indicate that CI-A was initiated around 2000 and CI-B and CI-C were initiated near 2145. These are the three groups of cells that we will focus on in this paper.

3. Numerical Model, Data and Experiment Design

[14] Version 5 of ARPS [*Xue et al.*, 2000, 2003, 2001] is used in this study. The ARPS is a general-purpose

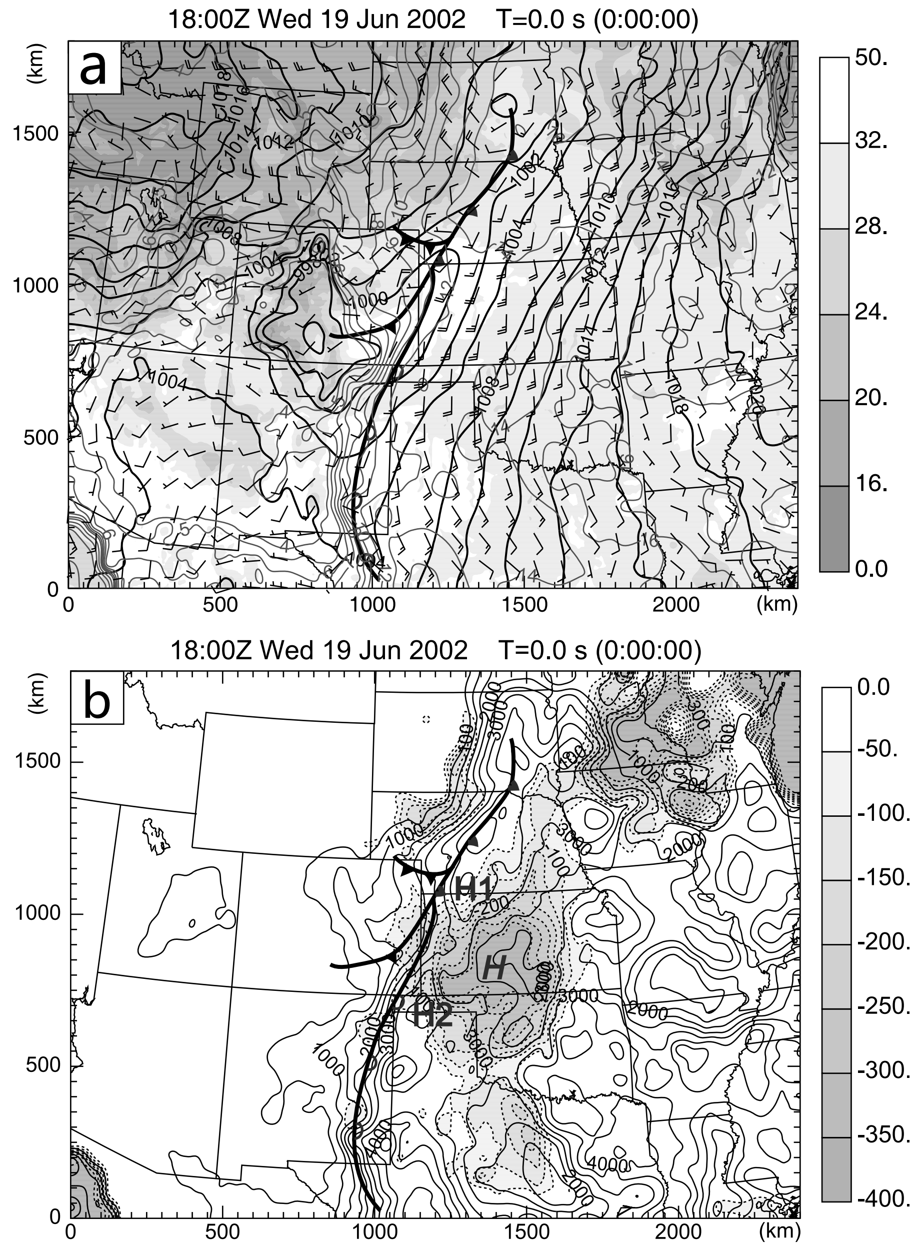

Figure 2. The surface fields at 1800 UTC 19 June 2002: (a) Mean sea level pressure (thick black contours, hPa), temperature (shaded, °C), water vapor mixing ratio (thin black contours, g kg^{-1}), and the wind field (full barb represents 5 m s^{-1}, half barb 2.5 m s^{-1}); (b) CAPE (contours, at 500 J kg^{-1} intervals, with maximum centers near triple point marked by H1 and H2), and CIN (dashed contours with gray shading, at 50 J kg^{-1} intervals, with the maximum center close to the dryline marked by *H*). Cold front and dryline are marked by standard symbols. These fields are from the ARPS 3DVAR analysis incorporating local data sets using the Eta analysis valid at the same time as the background.

nonhydrostatic atmospheric model suitable for mesoscale and convective-scale simulation and prediction. A model domain of 1003 × 1003 horizontal grid points with a 1-km grid spacing is nested inside a 3-km grid of 803 × 603 horizontal grid points (Figure 4). In the vertical, 53 stretched levels are defined on a generalized terrain-following coordinate, with the grid spacing increasing from about 20 m near the ground to about 800 m near the model top at about 20 km height. The model terrain and land surface characteristics on the 3- and 1-km grids are derived from 1-km databases. The lateral boundary conditions (LBCs) for the 3-km grid are from time-interpolated 6-hourly National Centers for Environmental Prediction (NCEP) Eta Model analyses interleaved by 3-h forecasts, while the 1-km grid gets its LBCs from the 3-km forecasts at 10-min intervals. Our earlier sensitivity experiments showed the benefits of using the relatively larger (53) number of vertical levels and high near-surface vertical resolution.

[15] The ARPS is used in its full physics mode [see *Xue et al.*, 2001]. The microphysics scheme is the *Lin et al.*

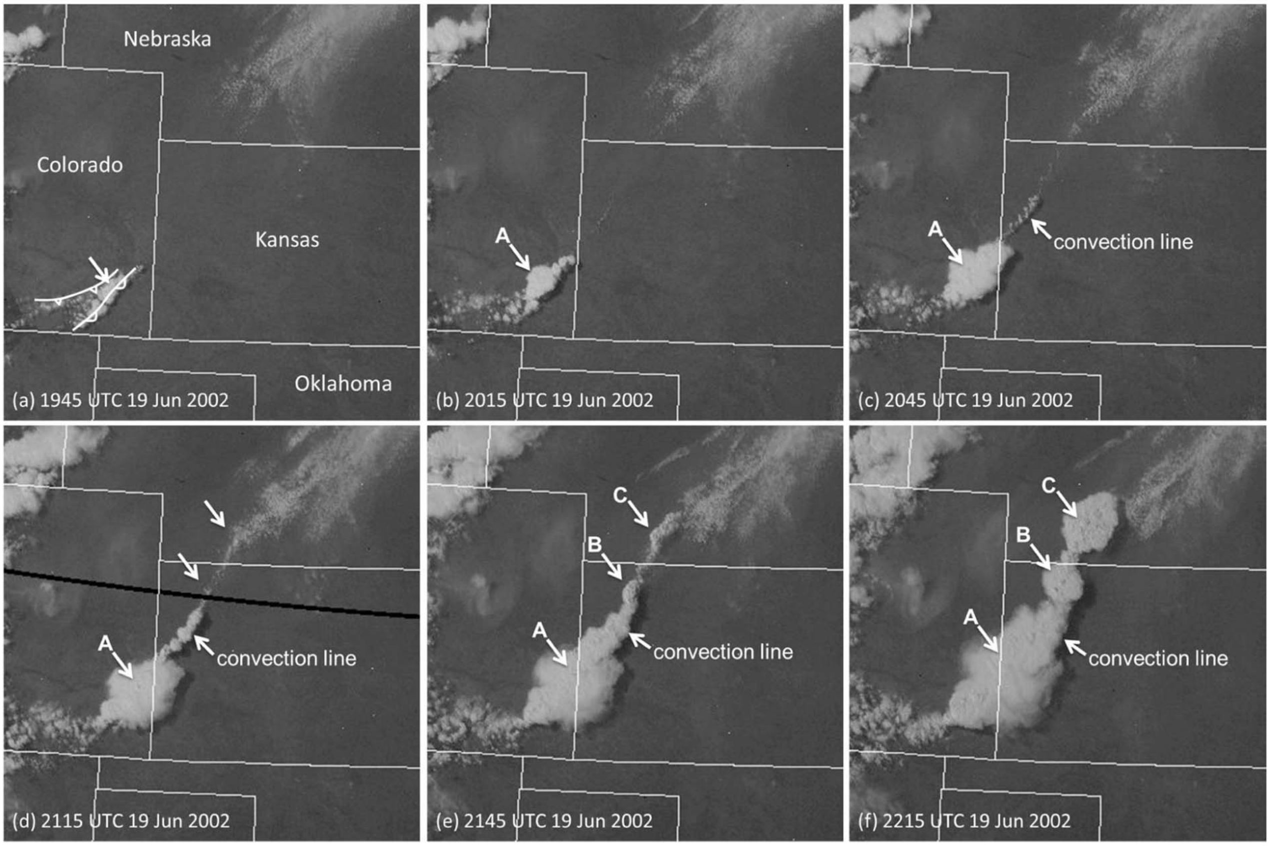

Figure 3. GOES visible satellite images taken at (a) 1945, (b) 2015, (c) 2045, (d) 2115, (e) 2145, and (f) 2215 UTC 19 June 2002. White downward arrows point to where three groups of cells (A, B and C) first form.

[1983] three-ice scheme. The 1.5-order (turbulent kinetic energy) TKE-based subgrid-scale turbulence parameterization and TKE-based non-local PBL-mixing parameterization [*Sun and Chang*, 1986; *Xue et al.*, 1996] are used. Also used is the NASA GSFC long- and shortwave radiation packages [*Chou*, 1990, 1992; *Chou and Suarez*, 1994], and the land surface condition is predicted by a two-layer soil-vegetation model initialized using the soil state variables presented in the Eta analysis. More details on these packages can be found in *Xue et al.* [2001].

[16] The initial condition of our simulations was created using the ARPS three-dimensional variational (3DVAR) data analysis scheme [*Gao et al.*, 2004]. The 3DVAR analysis was performed on the 3 km grid at 1800 UTC, 19 June 2002, using an NCEP Eta model analysis as the background. As in LX08, conventional forms of data are assimilated into the model initial condition, including those of regular and special mesonet surface stations, specially launched upper-air soundings, and wind profiler data. Available aircraft data, i.e., the Meteorological Data Collection and Reporting System (MDCRS) data, are also included. We did not include, however, special IHOP observations from mobile in situ or remote sensing platforms, because of their limited spatial and/or temporal coverage.

[17] Table 1 lists the standard and special data sets used, together with their key characteristics. These data sets are similar to those used in LX08, except for the additional 11-station ARM surface data used here. Figure 4 marks most of the observation sites used in this study. Data from six WSR-88D radars marked in Figure 4 are used for verification. For the IHOP-specific measurements, dropsonde data are used in the verification in section 4b. Table 2 lists the observations analyzed and the horizontal and vertical background-error decorrelation scales (radii) for each analysis pass in ARPS 3DVAR. As in our earlier studies, a multipass procedure is used, following earlier studies [e.g., *Hu et al.*, 2006; XM06a; XM06b; LX08], to allow for effective use of observations from networks of different density. The vertical decorrelation scale is defined in terms of the number of vertical grid levels.

[18] After an initial condition is obtained at 1800 UTC on the 3-km grid, the ARPS model is integrated first for 18 h until 1200 UTC 20 June 2002 on the 3 km grid. The 1-km grid forecast of the same length starts from interpolated 3-km analysis, using 10-min interval 3-km forecasts as the boundary conditions. We will present results on the 1-km grid only in this paper.

4. The Forecast of the Three CI Groups

[19] In this section, we will present the forecast results of the three groups of cells and their comparison with radar observations, with the goal of establishing the credibility of model predictions. The model prediction of the mesoscale

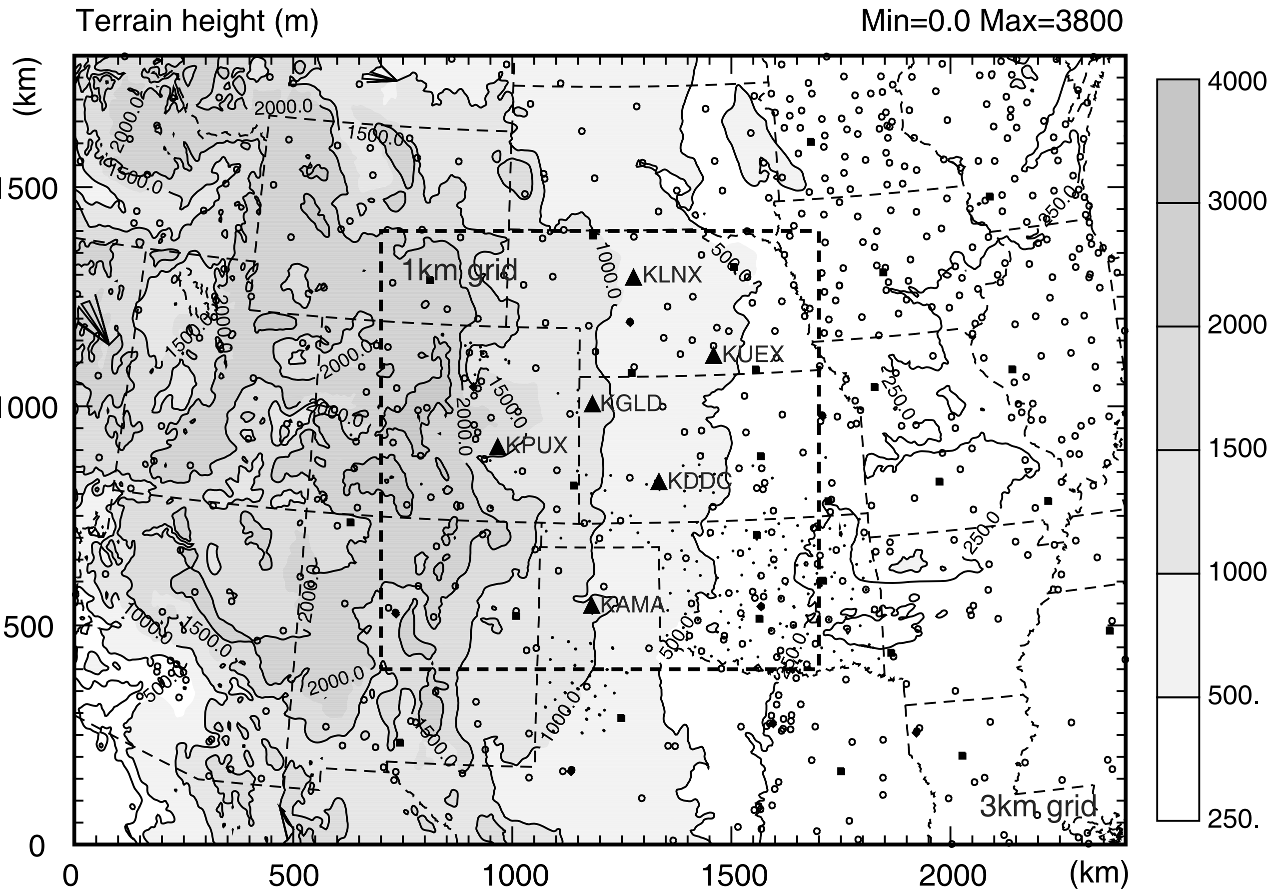

Figure 4. The 3-km model domain with terrain elevation shaded. The nested 1-km domain is indicated by the dashed rectangular box. The filled triangles indicate the radar locations of KLNX, KUEX, KGLD, KPUX, KDDC, and KAMA; the stations of the Oklahoma Mesonet, the West Texas Mesonet, the southwest Kansas mesonet, the Kansas groundwater management district #5 network, and the Colorado agricultural meteorological network are marked by small dots; the stations from ASOS and the FAA SAO are marked by circles; the stations from the NWS radiosonde network are marked by filled squares; and the stations from the NOAA wind profiler network are marked by filled diamonds. Also shown are state boundaries.

Table 1. List of the Abbreviations of the Observation Networks Used in This Study and Some of Their Characteristics

Type of Data Set	Abbreviation	Description	Temporal Resolution	Special or Standard	Number of Stations
Upper-air data sets	RAOB	NWS radiosonde network	3 h	data at 1200 are standard, others are considered special	30 at 1200 missing at 1500 11 at 1800
	WPDN	Wind Profiler Demonstration Network	1 h	standard	30
	COMP[a]	Special composite data set composed of many upper-air observing networks	1 h	special	1
	MDCRS	NWS Meteorological Data Collection and Reporting System aircraft observations	1 h	special	varies
Surface data sets	SAO	Surface observing network composed of the ASOS and the FAA surface observing network	1 h	standard	about 286
	COAG	Colorado Agricultural Meteorological Network	1 h	special	29
	OKMESO	OK Mesonet	1 h	special	about 138
	SWKS	Southwest Kansas Mesonet	1 h	special	8
	GWMD	Kansas groundwater Management District #5 Network	1 h	special	10
	WTX	West Texas Mesonet	1 h	special	30
	ARM	Atmospheric Radiation Measurement Southern Great Plains Surface Meteorological Data	1 h	special	11

[a]A description on the individual networks included in the composite can be found in *Stano* [2003].

Table 2. List of Analyzed Observations and the Horizontal and Vertical Filter Length Scales Used by Each Pass of the ARPS3DVAR Analysis

Pass Number	Analyzed Observations	Horizontal Decorrelation Scale (km)	Vertical Decorrelation Scale (Number of Grid Points)
1	RAOB, WPDN, COMP, and MDCRS	320	4
2	RAOB, WPDN, COMP, MDCRS and SAO	160	4
3	SAO, COAG, OKMESO, SWKS, WTX, GWMD and ARM	80	2
4	SAO, COAG, OKMESO, SWKS, WTX, GWMD and ARM	50	2
5	COAG, OKMESO, SWKS, WTX, GWMD and ARM	30	2

environment and the roles of various mesoscale features in the CI will be discussed in the next section.

4.1. The General Forecast of Three CI Groups

[20] In Figure 5, the model-predicted composite (column maximum) reflectivity fields and surface wind vectors are compared against corresponding radar and surface wind observations at 2000, 2100, 2200, and 2300, 19 June 2002. Here, the model reflectivity is derived using the formula defined in *Tong and Xue* [2005] from predicted rainwater, snow, and hail mixing ratios. The observed version is derived from observations of the six radars labeled in Figure 4. The three regions where CI-A, CI-B, and CI-C started and subsequently developed into convective storms are framed inside three small boxes, located respectively over southeast Colorado, northwest Kansas, and south-central Nebraska (Figure 5). Zoomed-in plots will be shown later for these regions.

[21] At 2000, radar observations show convective storm A near the southeast corner of Colorado (Figure 5a). In the model, a similar storm is seen at this time in forecasts (Figure 5e). By 2100, storm A started to show roughly three identifiable reflectivity cores in observation in a southwest-northeast lineup (Figure 5b) while the forecast also shows a new cell southwest and northeast of the initial cell, respectively (Figure 5f), although the southwest one is biased toward the west.

[22] By 2200, a thin convection line barely visible at 2100 in the observed reflectivity field to the northeast of cell group A (Figure 5b) had developed into a strong solid line echo (Figure 5c) while cells B and C had also been initiated, with C being stronger. The convection line and cell B have formed in the forecast although cell C has not formed (Figure 5g). Within and near the box of cell C, weak echoes are found in the forecast at this time; these echoes are associated with high-level clouds that quickly dissipated afterwards (Figure 5h) and are therefore not associated with any low-level initiation.

[23] By 2300, the observed cells B and C had undergone remarkable development (Figure 5d); they have essentially merged and formed a solid line that is now the strongest feature in the domain of interest. Cell A as well as the convection line had become weaker by this time. The overall convection line hardly moved between 2200 and 2300, being linked to a quasi-stationary dryline. In the model, the predicted cell C is at about the right location but is somewhat weak (Figure 5h); the delay in its initiation has contributed to this weaker intensity (compare Figure 5g and Figure 5c). Cell B and the convection line are over-predicted in intensity, while their locations are predicted quite well. In Figure 5, simulated surface winds also agree with observed winds well. In the following we discuss the time evolution of the three cell groups in more detail. Impatient readers who are willing to accept the modeling results as being realistic enough can jump to the last paragraph of section 4d then section 5, without too much loss of readability.

4.2. CI Group A

[24] Figure 6 shows the same fields as Figure 5 but inside the small squared box containing CI group A around its time of initiation. At 1930 (Figure 6a), radar observation shows initial weak echoes near the northern border of the Baca County, which developed into strong cells over the next hour and moved northeastward (Figures 6b and 6c). In the model, two clusters of cell are found along the cold front in southwest Otero County, and along the dryline in the Las Animas County (Figure 6d); these cells developed upstream 45 min earlier and are considered spurious; based on their initial location, they are not considered to be associated with CI group A. In the model, a cell formed in southeast Bent County at 2000 (denoted A in Figure 6e) that developed into the dominant cell by 2030 (Figure 6f); we designate this cell as the one that corresponds to the observed cell A based on its initial location and later evolution. The initiation of this cell is delayed by about 20 min compared to the observation but its initiation location is within 5 km of observation.

4.3. CI Group B

[25] Figure 7 shows the fields within the small box associated with cell group B (Figure 5). To avoid the interference of the short-lived upper level clouds (cf. Figure 5) with our examinations of low-level CI, simulated composite reflectivity as the column maximum below 6 km are shown in Figure 7 and Figure 8. Around 2140, an isolated cell, identified as cell B, with observed reflectivity exceeding 35 dBZ first appeared at central Thomas County, Kansas (Figure 7a). Over the next 20 min, this cell intensified and its reflectivity core reached the eastern Thomas-Rawlins border (Figure 7b). By 2230 (Figure 7c), cell B further strengthened and joined up with rapidly developing convective cells to its northeast that was the southwest extension of cell group C (cf. Figures 5 and 3), to form a connected line. During this period, the convection line to the southwest of cell B also exhibited growth.

[26] Detailed comparisons show that the model predicted initiation of cell B is about 30 min later than observed (Figures 7d–7f), and about half a county too far east. At 2140 (Figure 7d), the model first predicts a small isolated echo in western Sheridan County, at the eastern edge of the surface dryline. East of the dryline are southerly winds. The dryline extends north to the northeastern corner of Decatur

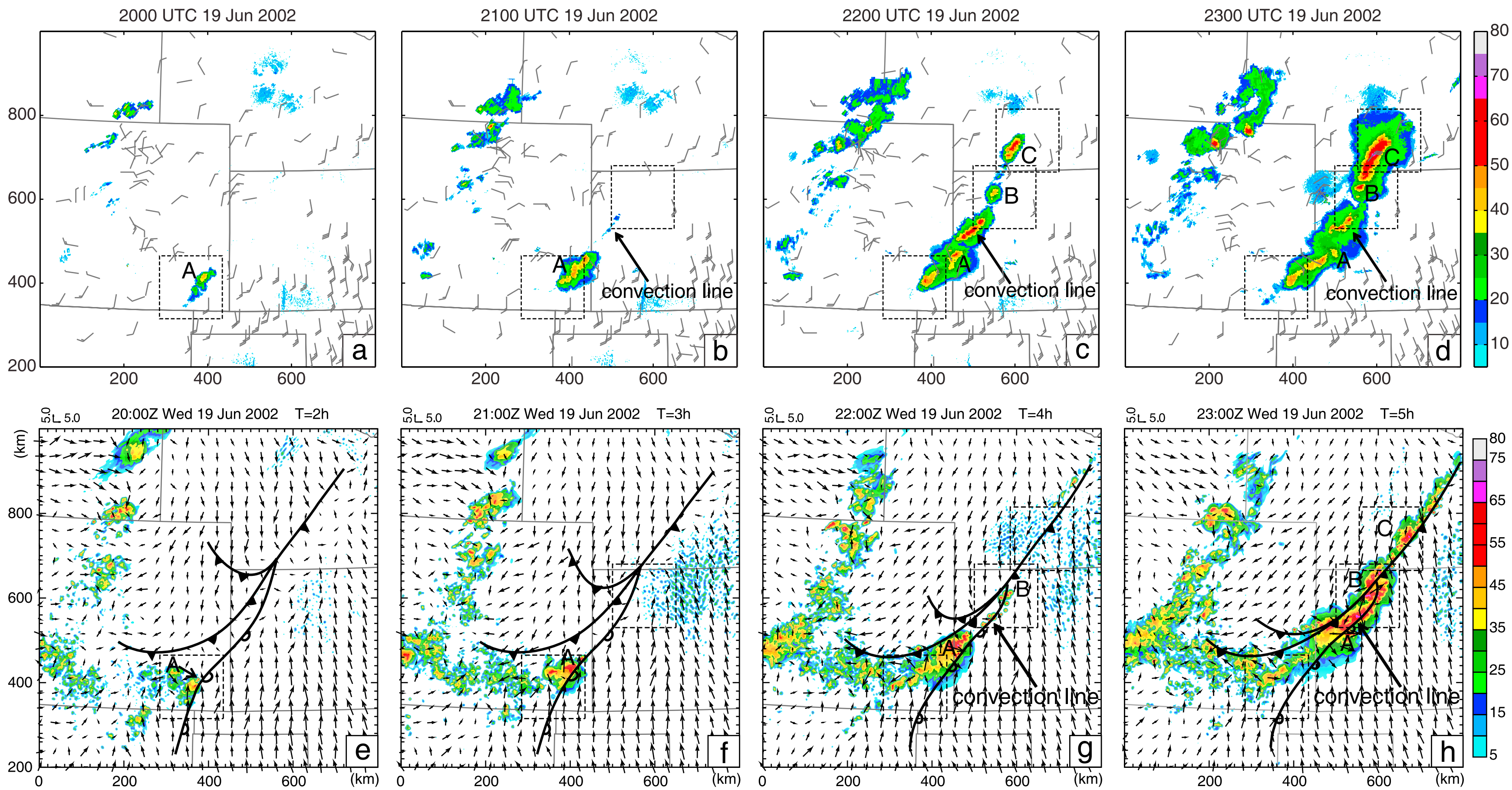

Figure 5. Observed composite reflectivity fields and surface wind barbs (full and half barbs represent 5 and 2.5 m s^{-1}, respectively) at (a) 2000, (b) 2100, (c) 2200, and (d) 2300 UTC 19 June 2002. (e–h) are the same as Figures 5a–5d but for the corresponding ARPS 1-km forecast composite radar reflectivity (color shaded) of control data assimilation experiment. Cold front and dryline are marked by standard symbols in Figures 5e–5h.

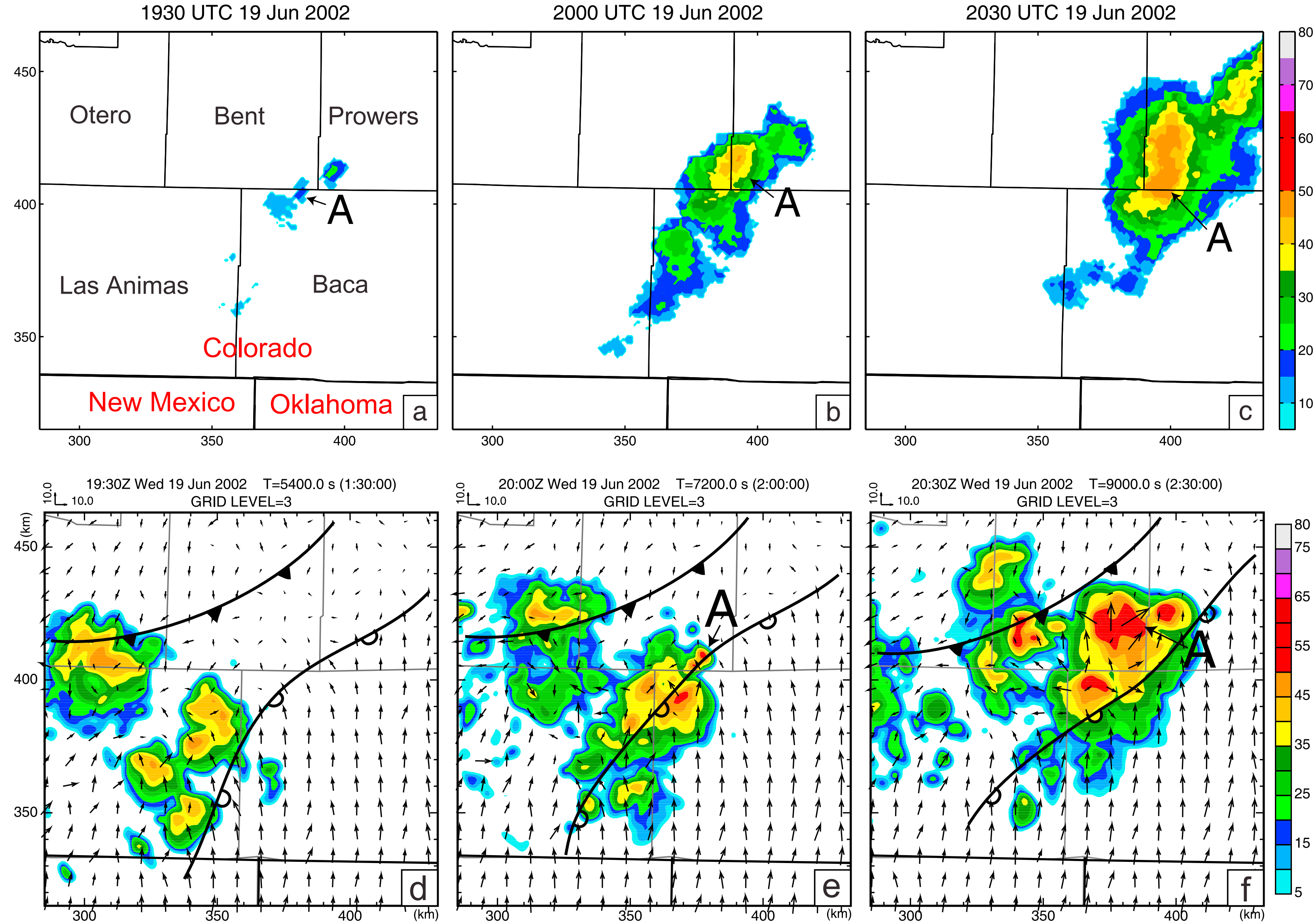

Figure 6. Observed composite reflectivity fields (color shaded) at (a) 1930, (b) 2000, and (c) 2030 UTC 19 June 2002 and (d–f) the corresponding 1-km forecast composite reflectivity, together with forecast wind vectors at about 30 m AGL. Relevant counties and states are labeled in Figure 6a. The domain corresponds to the square box over southeastern Colorado in Figure 5, over the region of CI-A.

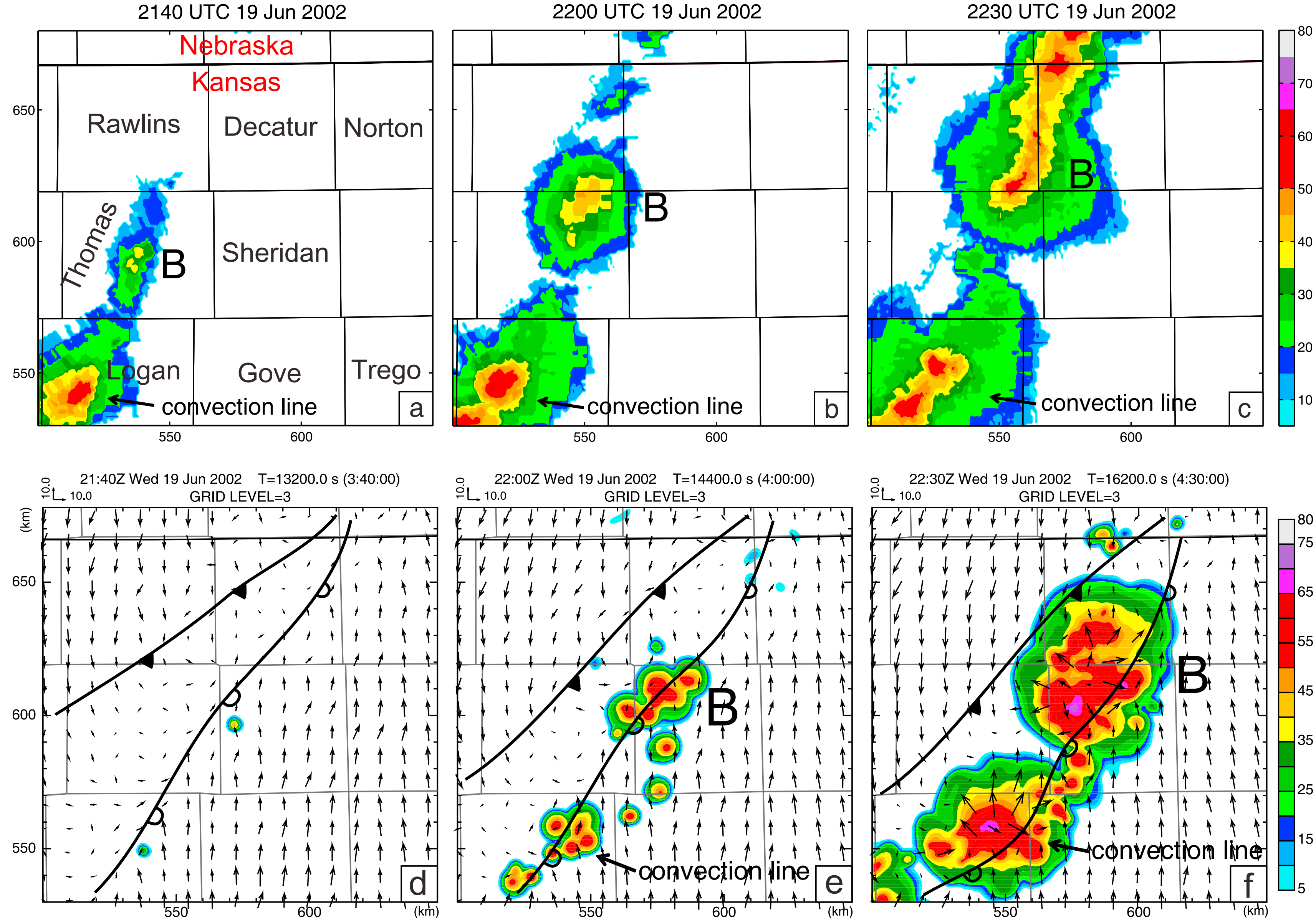

Figure 7. Same as in Figure 6, but for CI-B with observation fields at (a) 2140, (b) 2200, and (c) 2230 UTC 19 June 2002, and (d–f) forecast fields valid at the corresponding times. The observed and simulated cell B is labeled. Counties and states are labeled in Figure 7a. The domain corresponds to the small square box over northwest Kansas in Figure 5.

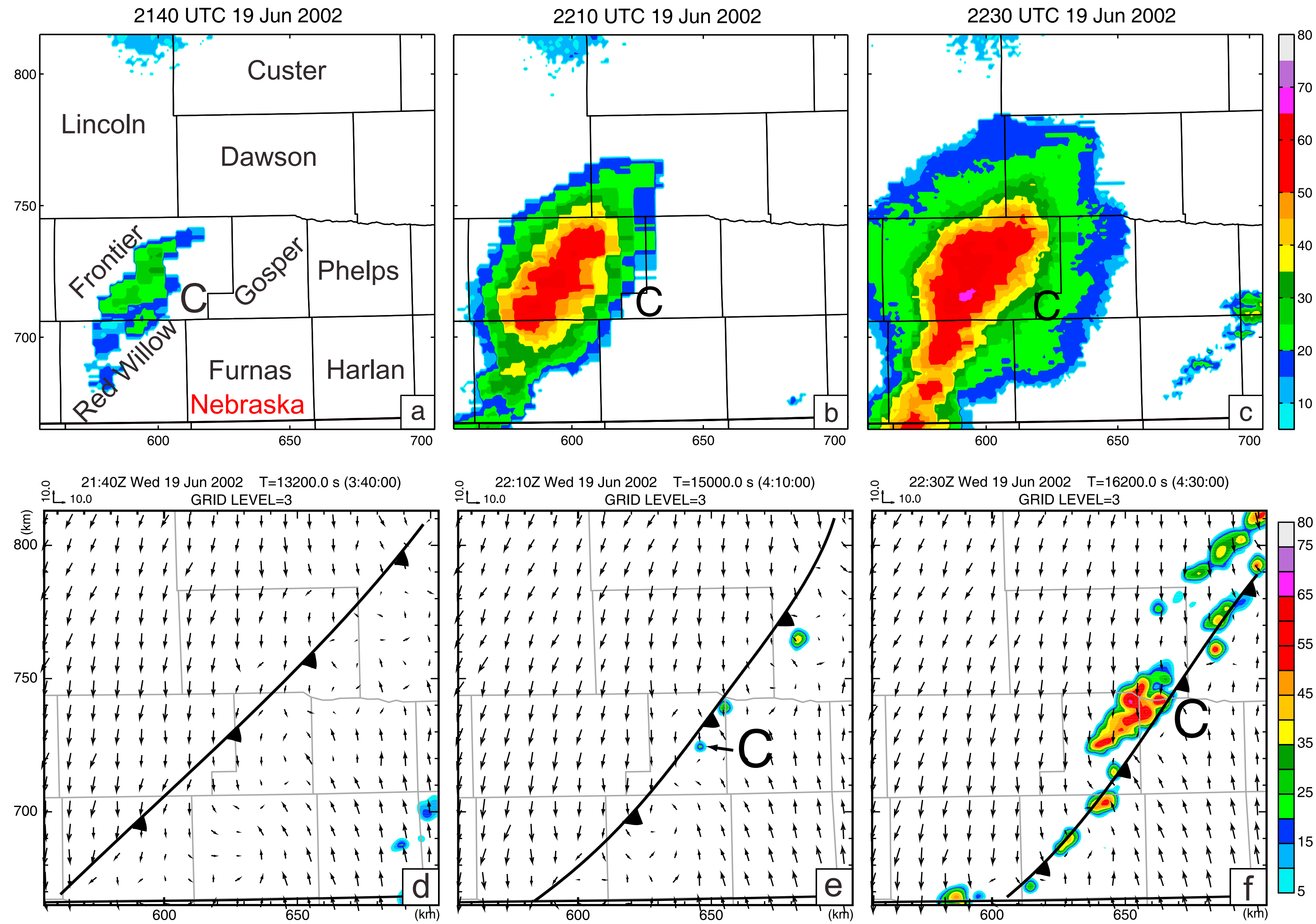

Figure 8. The same fields as in Figure 6, but for CI-C with the observation fields at (a) 2140, (b) 2210, and (c) 2230 UTC 19 June 2002, and (d–f) the forecast fields valid at the corresponding times. The observed and simulated cell C is labeled. Counties and states are labeled in Figure 8a. The domain corresponds to the square box over south-central Nebraska in Figure 5.

County where it intercepts the cold front that extends west-southwestward to the Thomas-Rawlins border. By 2200 (Figure 7e), the isolated cell in Sheridan has grown in size, and acquired a few smaller cells around it; the cell group has a good general correspondence with the observation (Figure 7b). To its southwest along the dryline, another group of cells had also developed, which corresponds to the northern end of the observed convection line (cf. Figure 5). By 2230, these cells gained intensities and area coverage that are somewhat larger than observed (Figure 7f versus Figure 7c). The overall orientation of the convection organization is southwest to northeast, in agreement with observation, while the overall line is displaced eastward by about 50 km, similar to the displacement at the earlier initiation time. We note that the details of the simulated reflectivity structure can be sensitive to model microphysics; using the two-dimensional of the ARPS model, *Wakimoto et al.* [2004] found that in idealized simulations for convection associated with group B of this case, modifications to the *Lin et al.* [1983] ice microphysics scheme in the ARPS resulted in a better match of the simulated reflectivity to observations.

4.4. CI Group C

[27] Cell group C occurred further north where the dryline ceases to exist, and where southerly and northerly flows directly oppose each other at the surface cold front (Figure 8). At 2140 (Figure 8a), the observed initial convection was over Frontier County, Nebraska. In the next 60 min (Figures 8b and 8c), this cell showed rapid development, and formed an intense line-shaped convection of a significant width by 2230.

[28] The model initiation is again delayed by about 30 min compared to observations and there is an eastward displacement of the predicted convection relative to the observation. The model first predicted the echo associated with cell C at around 2210 (Figure 8e), and about 60 km east of the observed location (cf. Figure 8a). Over the next 20 min, new cells are initiated southwest and northeast of the initial cell and gradually merged with the initial cell similar to observed. By 2230 (Figure 8f), a short line structure is established. Additional small cells further developed to the south and north of this line, all along the convergence zone associated with the cold front (Figure 5d). The displacement of this as well as the earlier group B suggests that the model prediction of the cold front and dryline has 50 to 60 km position error.

[29] Overall, despite differences in structural, timing and position details, there is clearly identifiable correspondence between the model and observation for each of the three cell groups; this establishes the credibility of the model simulation so that further analyses on the model output can be performed with a certain degree of confidence. In the next section, we will analyze the mesoscale environment and associated processes that support and initiate convection.

5. The Prediction of Mesoscale Environment and Its Relationship With CIs

5.1. Evolution of Predicted Cold Front and Dryline Near the Surface

[30] The model surface winds and water vapor mixing ratio (q_v) are plotted in Figure 9 for 1800, and for the times when 10–20 dBZ echoes corresponding to each of the three CIs were first predicted. The surface cold fronts, including a secondary front behind the primary one, are drawn in standard frontal symbols. A dryline is analyzed along the zone of strong moisture gradient east of the primary cold front which intercepts the cold front in northwestern Kansas. The secondary cold front is at the leading edge of an even colder (cf. Figure 2a) but moister air mass coming in behind the primary cold front. In Figure 9, the white filled squares A, B, and C mark the locations of model initiation of the three cell groups. Despite the position errors of modeled features, here we are most interested in their relative positioning and general physical realism.

[31] The surface fields changed remarkably during the period shown (Figure 9). By 1950 (Figure 9b), the moisture field developed many small-scale structures due to boundary layer (BL) convective activities including horizontal convective rolls and open cellular convection (XM06a, XM06b). The primary cold front in northwestern Kansas advanced southward somewhat, making the dry air wedge between the dryline and cold front narrower. CI-A was first initiated at this time, immediately to the west side of the 10 g kg^{-1} moisture contour near the dryline. Note that the air behind the secondary cold front spread southwestward (Figure 9b), advancing into northeast Colorado, establishing a major S-shaped moisture boundary (one can follow the green region between 11 and 12 g kg^{-1} moisture contours) with the lower part of ‘S’ later developing into a dry tongue structure over northwest Kansas, as described in the observational study of M06.

[32] By 2138 (Figure 9c), the northerly and northeasterly winds behind the secondary cold front pushed the front further into northwest Kansas; its eastern portion has essentially caught up with the primary cold front. Meanwhile, the dryline remained more or less stationary. The dryline also exhibits a somewhat wavy pattern that was noticed by M06 in the Goodland Kansas WSR-88D radar data, due to the eastward push in the north by the cold front and westward push by the southerly flows east of the dryline. The model-predicted CI-B was initiated at this time at the dryline, and near the tip of the dry tongue which is also the triple-point between the cold front and dryline. The associated initiation process will be further analyzed and compared with observations later. By this time, cell group A has fully developed, and produced divergent flows and cold pool at the surface.

[33] Over the next 30 min or so, the cold front remained quasi-stationary. Near 2210, cell C was initiated along the cold front, at a point where surface moisture appears to be enhanced (Figure 9d). Changes in the near surface moisture field will be further discussed later.

5.2. Evolution of Vertical Structures Around the Dryline and Cold Front

[34] To understand the interactions among the dryline, cold front, and associated flows as well as the embedded small scale structures at the times of CI, we examine fields in vertical cross sections through the initiation points that are roughly normal to the dryline or cold front. Equivalent potential temperature (θ_e) and wind fields projected onto the cross sections are shown in Figure 10 (to focus on mesoscale structures, the fields were smoothed before plotting), at

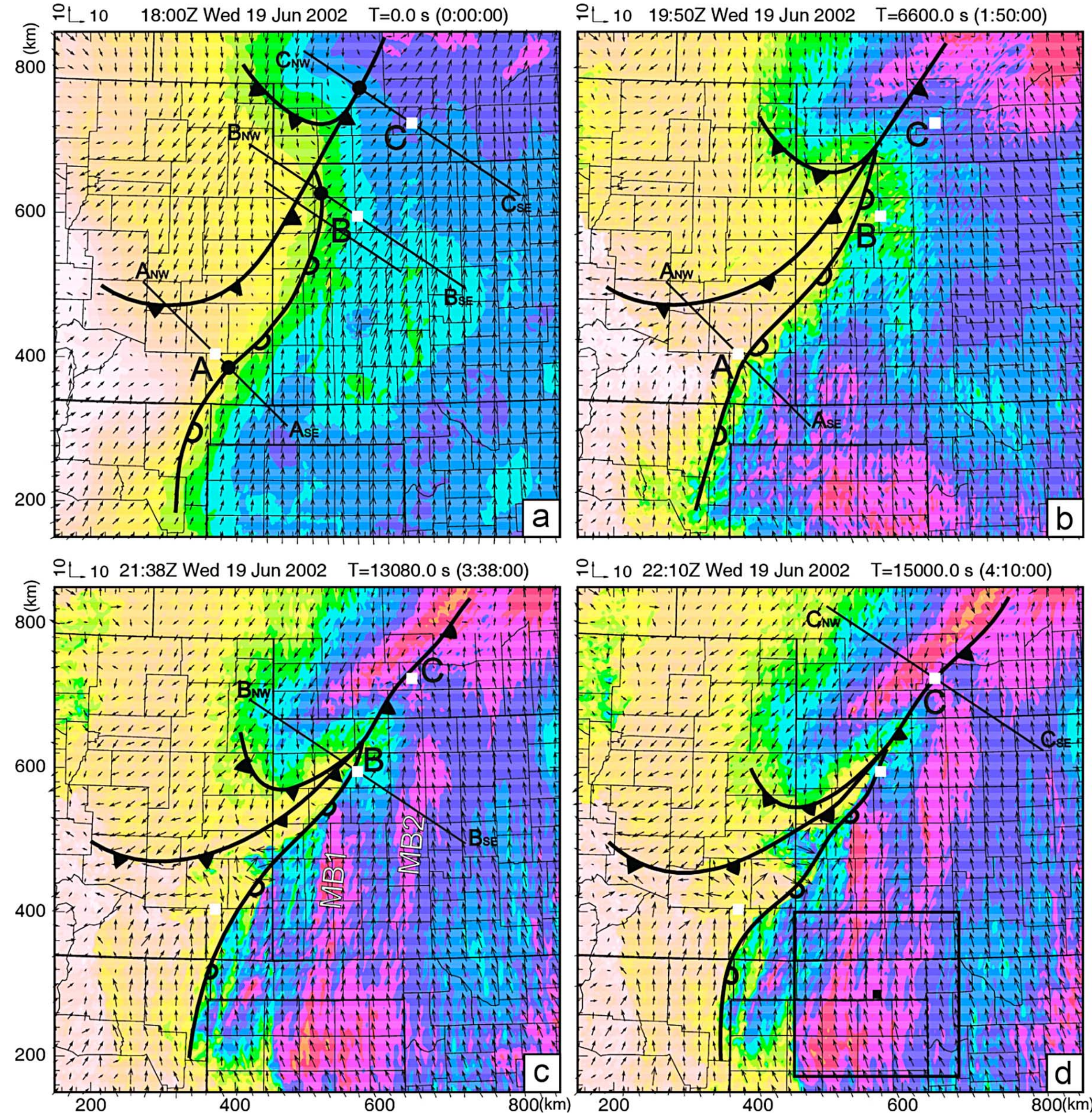

Figure 9. Surface q_v (shaded, g kg^{-1}) and wind fields (vector unit shown in the plots, m s^{-1}) at (a) the initial condition time, (b) 1950, (c) 2138, and (d) 2210 UTC 19 June 2002. The times of Figures 9b–9d correspond to the minutes that 10~20-dBZ composite reflectivity contours first appear for storm cells of the three CIs. The labels A, B, and C mark the locations (white squares) where the CI-A, CI-B, and CI-C first initiates. Black dots in Figure 8a denote the locations of soundings shown in Figures 12a, 12c and 12e. Cold front and dryline are outlined in standard symbols. Thick black lines cross A, B, and C indicate locations of vertical cross sections shown in Figure 10. The box over Oklahoma panhandle in Figure 8d denotes the region of NCAR S-pol radar reflectivity observations shown in Figure 19 and the black square at the center is the location of the S-pol radar.

times and locations indicated in Figure 9. Also shown in these cross sections are the air mass boundaries in thick dashed lines, subjectively analyzed based on the wind directions in the cross sections and in reference to Figure 9. The thickened 333 K θ_e contours roughly correspond to the BL top; the upward arrows in Figures 10a, 10c, and 10e denote the positions of dryline or cold front found in Figure 9a.

5.2.1. Vertical Structures Near CI-A

[35] At 1800, along cross section A_{NW}–A_{SE} in Figure 9a, the flow and θ_e structures are typical of drylines (Figure 10a). A shallow layer of higher θ_e air is confined to the lowest 1–2 km layer east of the dryline, containing a

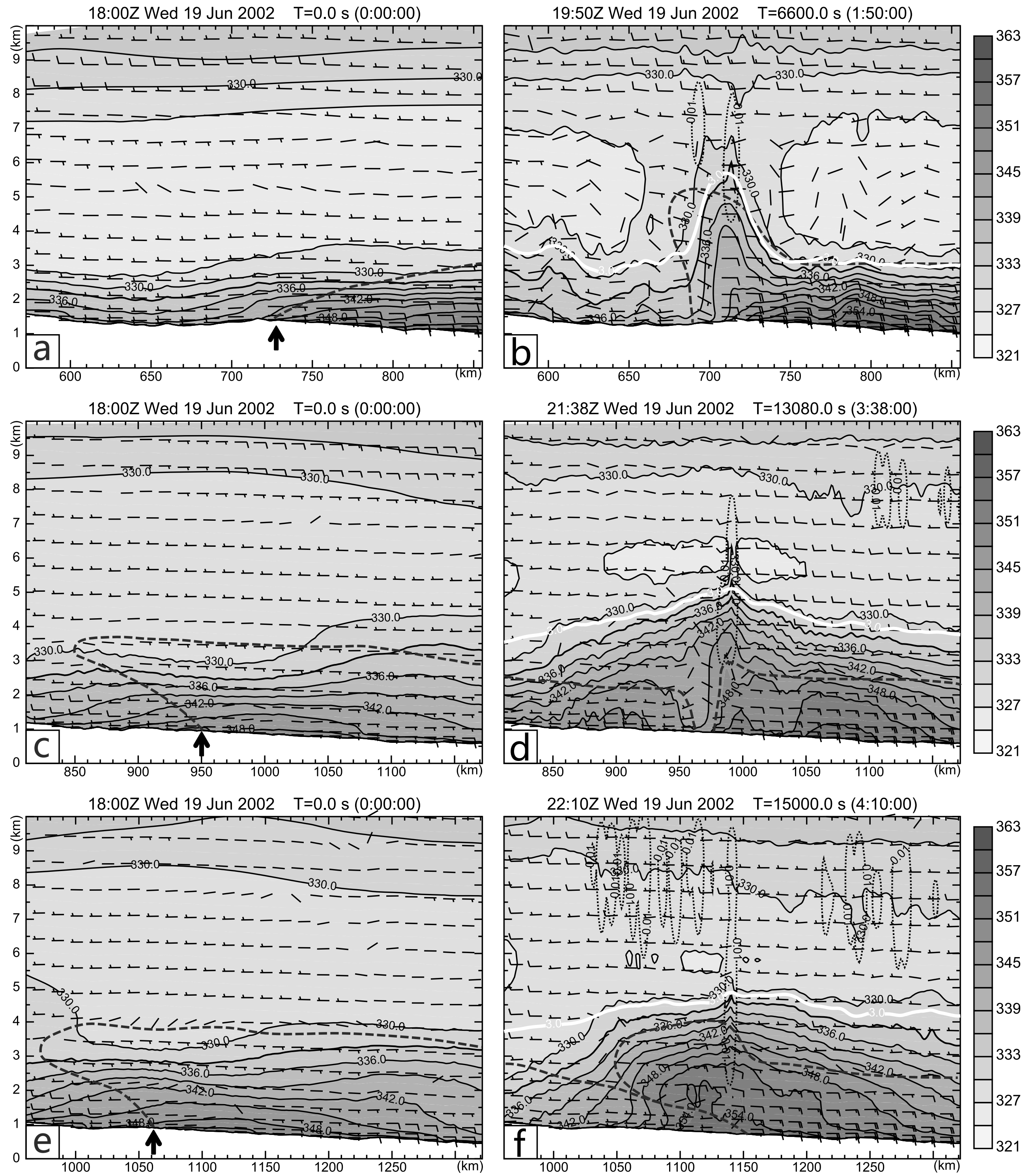

Figure 10. Vertical cross sections plotted along lines (a and b) A_{NW}-A_{SE}, (c and d) B_{NW}-B_{SE} and (e and f) C_{NW}-C_{SE} in Figure 9, for the initial condition time (1800, Figures 10a, 10c and 10e), and the times of CI-A, CI-B and CI-C (Figures 10b, 10d and 10f). Plots are equivalent potential temperature (θ_e shaded with contours, K), horizontal vector winds projected to the cross section (wind barbs), and the 0.01 g kg^{-1} total condensed water/ice outlining the clouds (dotted contours). The 333 K θ_e contours are thickened. The thick dashed lines outline the air mass boundaries, analyzed mostly based on the wind directions. Upward arrows in Figures 10a, 10c and 10e denote the positions of the dryline in Figures 10a and 10c and cold front in Figure 10e, also the sounding locations in Figures 12a, 12c and 12e. The white contour is for the 3 g kg^{-1} water vapor mixing ratio. Two dimensional smoothing was applied to the fields before plotting.

southeasterly wind component. The dryline separates the lower θ_e air at surface which also over-rides the higher θ_e air about 1 km AGL. At this time, no upward θ_e bulge is evident. Figure 9a shows that this cross section actually extends into the cold air behind the cold front, but the change in the thermodynamic property of air across the front is relatively small.

[36] By 1950, the time of CI-A (Figure 10b), a notable upward θ_e bulge has developed in the dryline region, with the higher θ_e air reaching above the 5-km level. This θ_e bulge is due to the uplifting of moist air ahead of the dryline (Figure 9b). At the apex of this θ_e bulge a narrow column of cloud condensate (dotted contour) exists that extends to the 8 km level. The θ_e bulge exhibits a localized upward kink associated with the cloud column, which should be the result of enhanced upward motion there due to condensational heating.

[37] The time evolution of the BL structures can also be examined from model extracted soundings. These soundings are extracted at 1800 where the vertical cross sections intercept the dryline or cold front (black dots in Figure 9a), and at the CI times and locations as indicated by white open squares in Figure 9. At 1800, at the dryline location near the later CI-A, there exists a stable layer between 800 and 700 hPa, capping air underneath; the CIN for surface air parcel is 98 J kg^{-1} (Figure 12a). Between 700 and 450 hPa is a layer of neutral stability and low moisture content because of the high plateau origin of the air. By 1950 (Figure 12b), strong BL mixing has eroded the cap, and specific humidity is essentially constant below 570 hPa; the latter should be due to both BL mixing and the convergence lifting in the dryline zone. A saturated layer is found between 570 and 400 hPa, while surface-based LFC is at 600 hPa and CAPE reaches 2756 J kg^{-1}.

[38] To see if the convection might have acted to enhance the mesoscale θ_e bulge at this time, we rerun the model with the condensational process turned off; this prevents condensation from occurring even when super-saturation has been reached. The left column of Figure 11 shows the plots for the 'dry' run corresponding to the right column of Figure 10. It is clear that θ_e fields in Figure 10b and Figure 11a, including the mesoscale θ_e bulges, are very similar, except for the enhanced θ_e associated with the cloud column in the moist run. The effect of convection on the bulge is therefore very local at this time. Clearly, persistent BL convergence forcing at the dryline zone lifts the BL air, creating a mesoscale θ_e bulge, and the air at the apex of the budge first reaches saturation, rises above the LFC and sets off convection. The rise of the unstable moist parcels establishes the saturated layer seen in the sounding (Figure 12b). The 3 g kg^{-1} q_v contour shows a very similar moisture bulge as the θ_e bulge (Figure 10b), indicating that the θ_e bulge is mostly due to the elevated moisture in the bulge.

[39] One interesting question to ask: what is the role of surface heating in producing the moisture bulge and what if the heat flux is turned off? We reran the simulation with the surface heat flux turned off and plot the corresponding vertical cross-sections in the right column of Figure 11. Figure 11b shows that the θ_e and q_v bulges are clearly shallower, with the 333 K contour reaching only 4.7 km versus the 5.5 and 6 km in the dry and control runs, respectively. Also clearly evident is that the BL on both sides of the bulge is shallower than the cases with heating, and the vertical θ_e gradient is weaker in the latter cases, due to effects of vertical mixing. The surface heating can play two roles; it causes vertical mixing in the BL due to dry convective instability it creates, making the BL close to being neutrally stable and the BL air easier to lift in the dryline region, and the vertical mixing on both sides of the dryline can enhance surface convergence by bringing higher westerly and easterly momentum to the lower levels. It appears that both processes are active. Despite the difference in the boundary layer thermal structures in the non-heat-flux run, CI still occurred in the model at about similar time, however (Figure 11b). This is apparently because convection in this region started less than 1.5 h into the model run (cf. Figure 6) therefore the accumulative effect of surface flux is relatively small. The convergence at the dryline is sufficient to lift the parcels at the dryline to their LFC. The cells in region A are not as strong as in the heat flux runs later on (not shown).

5.2.2. Vertical Structures Near CI-B

[40] The flow structures in the cross section along B_{NW}–B_{SE} (Figure 9a) through CI-B are different from those of CI-A (Figure 10c). At 1800, this cross section roughly cuts through the dryline-cold-front triple point (located roughly at 950 km of the horizontal axis, cf. Figure 9), the classical dryline structure is therefore less evident. At this time, flow convergence along the cross section is weak (Figure 9a), and the warmer southeasterly flow component overrides the northwesterly component of cold air but the gradient of θ_e is relatively weak (Figure 10c). By 2138 when the cell B was initiated, the secondary cold front has advanced and merged with the main cold front, bringing in stronger northerly flow behind the cold front and enhancing the convergence (Figures 9c and 10d). In fact, three air masses can be identified at this time in this cross section, the air masses behind the front, ahead of the dryline, and that sandwiched in-between. The latter air mass has the lowest θ_e due to the lowest moisture content. A broad uplift of the BL air and a more symmetric upward θ_e bulge above the convergence zone are found associated with the strong low-level convergence between the southeasterly flow component ahead of the dryline and the northwesterly flow component behind the merged cold fronts (Figure 10d); this is clearly shown by the 333 K θ_e contour which more or less defines the top of the well-mixed BL. The CI again occurs right at the position of maximum upward θ_e bulge, feeding off the high θ_e air that is originated ahead of the dryline on the east (moist) side.

[41] For CI-B, the 1800 sounding at the cross-section near the dryline intercepting point (Figure 12c) has a similar structure as that at A point (Figure 12a) except for a stronger cap with a CIN of 157 J kg^{-1}. By 2138, the CIN is completely removed and below 650 hPa the atmosphere is neutrally stable. A saturated layer with temperature following the moist adiabat is seen between 650 and 470 hPa (Figure 12d), given that a convective cloud has formed (Figure 10d). In contrast, when the condensation is disallowed in the dry run, the corresponding sounding in Figure 13a shows a super-saturation layer near 650 hPa. Below that level, the atmosphere is neutrally stable to dry convection, and q_v is higher than 10 g kg^{-1}. The surface-based air parcel would reach its condensation level at 686 hPa which is essentially also the LFC. The CAPE of the

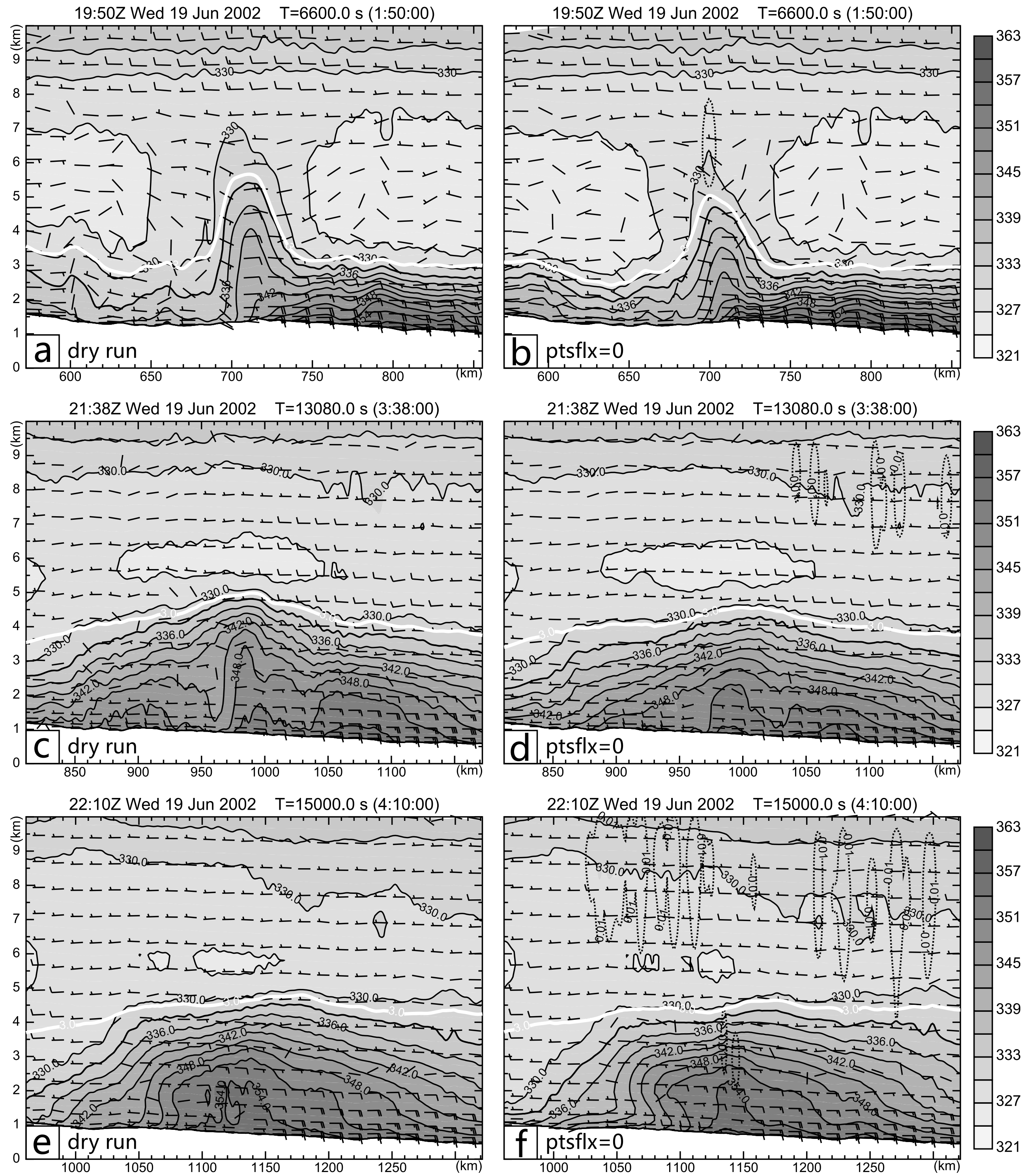

Figure 11. The same as Figures 10b, 10d and 10f, but for (a, c and e) the dry run and (b, d and f) the experiment with surface heat flux turned off.

sounding is 4114 J kg^{-1}, versus the 3229 J kg^{-1} of control run. Obviously, the artificial inhibition of condensation has allowed more CAPE to accumulate – if at this time condensation is turned on in the model, convection would surely fire up, starting with the saturated air near 650 hPa.

[42] In contrast, when the surface heat flux is turned off, a 28 J kg^{-1} CIN remains by 2138 (Figure 13b), and moisture does not get well mixed in the BL. The surface temperature is a few degrees lower than the heat flux case, but the CAPE of surface-based parcels is even larger (4494 versus 4115 J kg^{-1}) than the dry case (Figure 13a). This is because of the larger value of q_v at the surface in the former case, without the reduction by vertical mixing. In this case, CI in

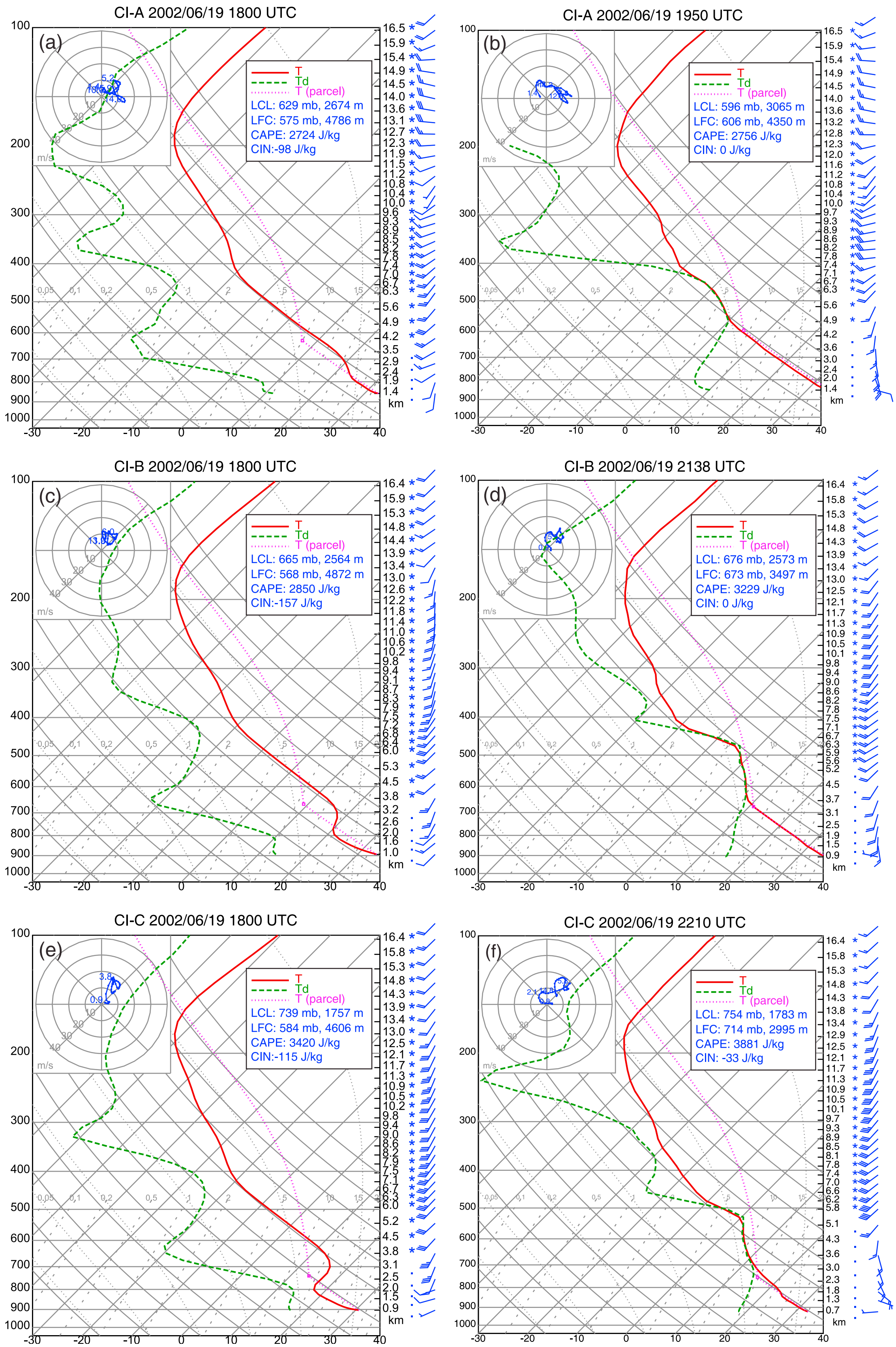

Figure 12. Skew-T plots of soundings extracted from model forecasts at 1800 at black dots lined with locations of (a) CI-A, (c) CI-B, and (e) CI-C in Figure 9a, and at (b) CI-A location at 1950, (d) CI-B location at 2138, and (f) CI-C location at 2210.

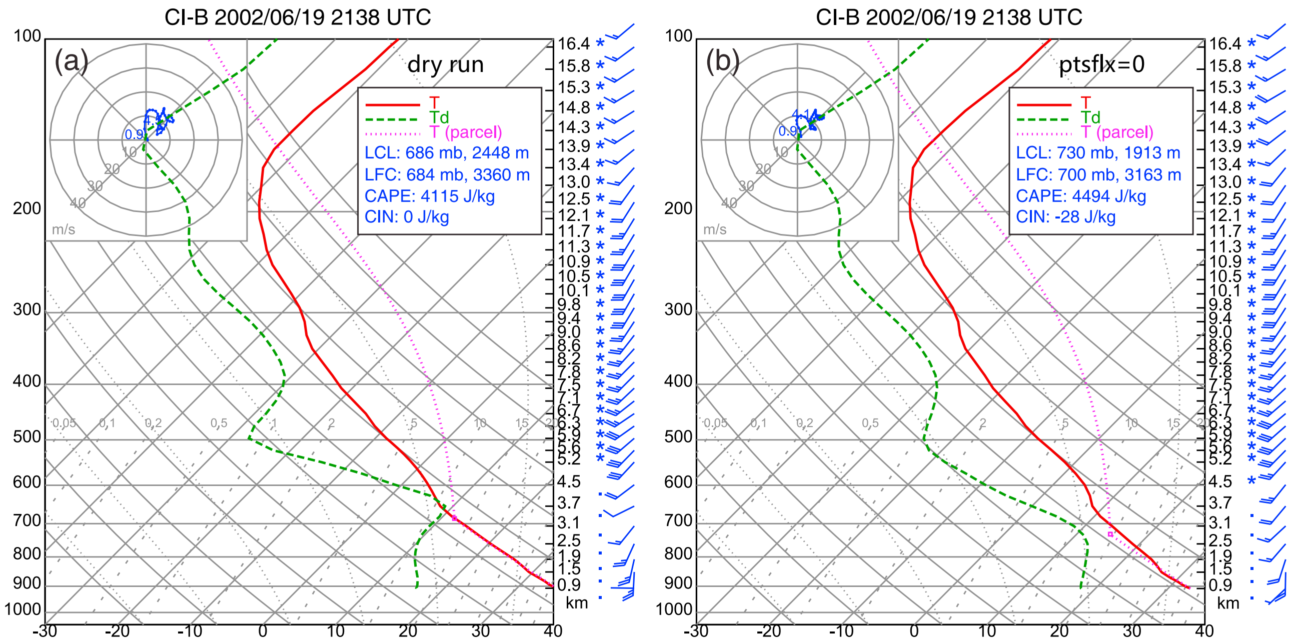

Figure 13. The same as Figure 12d, but for (a) the dry experiment, and (b) the experiment with surface heating flux turned off.

region B does not occur until 2230, and cells remain rather weak and last for only about one hour (not shown).

[43] The vertical cross section for the dry run for CI-B is again very similar to that of moist run, except for the lack of a localized kink at the crest of θ_e and q_v bulges and the lack of a cloud column there (Figure 11c). The bulges are noticeably weaker without surface heat flux (Figure 11d), with the 330 K θ_e contour reaching 4.2 km versus the 5 km in the dry case.

[44] One unique opportunity to verify the model prediction is presented by having a series of aircraft dropsondes deployed during IHOP between 2110 and 2132 (see Figure 3c of M06). The dropsonde path is roughly along a line 20 km south and 30 km west of line B_{NW}–B_{SE} and is drawn as a short straight line in Figure 9. The predicted horizontal winds, q_v, virtual potential temperature θ_v, and θ_e along this dropsonde cross section are plotted in Figure 14 and compared with the analyses from the dropsonde observations. Mixing ratios greater than 7 and 9 g kg^{-1} are shaded gray for the observations and model, respectively. To facilitate the comparison with the relatively smooth analysis fields, the model fields were smoothed before plotting, thereby removing small scale structures associated with BL dry convection.

[45] As discussed earlier, three distinct air masses can be identified (Figure 14), in both model and observations. The air mass behind the cold front was relatively cool and moist and had a persistent northerly flow up to 700 hPa. East of the dryline was a relatively moist air mass associated with southerly flows. Within these two air masses, the lowest layer of about 1 km depth is convectively unstable in the observation, due obviously to afternoon heating (Figure 14a). In the layer between 750 and 700 hPa, the atmosphere away from the dryline and front is very stable. This layer is also the boundary between the boundary layer air masses and the much drier and less stable air above; the latter has its origin from the western high plateau region and is what constitutes the dry air west of the dryline with much lower θ_e (Figure 14b). At the lower levels in-between the two air masses is what constitutes the dry tongue referred to earlier. In this region and the layer above, static stability is low, but the air is also very dry, hence unfavorable for moist convection.

[46] The features described above are well reproduced by the model, as we compare Figure 14c against Figure 14a, and Figure 14d against Figure 14b, despite about 30 min time difference in the fields plotted. The main difference is with the θ_v field in the lowest kilometer on the moist side; the model field does not show clear super-adiabatic lapse rate there (Figure 14c) as the observations do (Figure 14a). This is likely due to overly aggressive removal of instability there by resolved convection and the TKE-based nonlocal PBL parameterization scheme in the ARPS model. The fact that convective roll activities do exist in the model (not shown) suggests that surface heating in the model had definitely created near surface instability there.

[47] Again, the most prominent mesoscale features in the cross sections are the upward θ_e and q_v bulges (Figure 14). These bulges reach about 550 hPa in both observation and model, and the model indicates a localized narrow bulge about 30 km east of the surface dryline location that extends all the way from the surface to 6 km level (Figure 14d). This localized narrow bulge is linked to the CI at this time (cf. Figure 10d). The analysis from the aircraft dropsondes shows the bulges are of mesoscale and closely connected with two counter-rotating vertical circulations across the cold front and dryline boundaries, respectively [*Wakimoto and Murphey*, 2010]. Similar activity is happening in the model. The upward bulges produce a well-mixed BL up to ~650 hPa as in the observations.

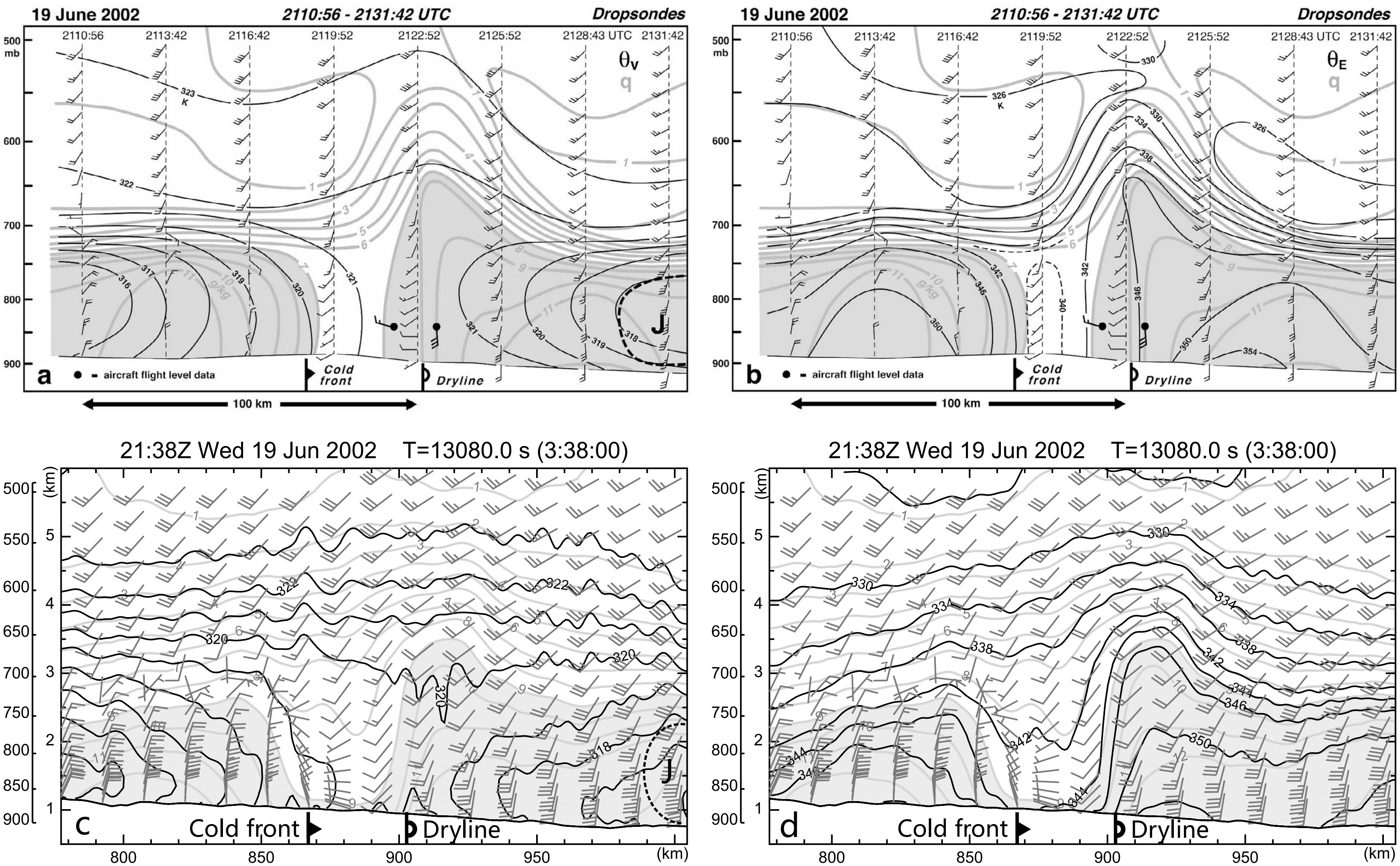

Figure 14. (a and b) Observed and (c and d) model-predicted horizontal winds, water vapor mixing ratio (gray lines) for the CI-B region, overlaid with virtual potential temperature (thick contours, Figures 14a and 14c) and equivalent potential temperature (thick contours, Figures 14b and 14d). The observational plots are based on a series of aircraft dropsondes along a straight flight path (reproduced from *Murphey et al* [2006]) and the cross section in model is located roughly along the flight path. The model fields were smoothed for easier comparison of mesoscale structures with observations.

[48] Similar moisture bulges associated with deep convergence and updrafts have been simulated [e.g., *Ziegler et al.*, 1997; XM06a; XM06b] and observed [e.g., *Schaefer*, 1974; *Ziegler and Hane*, 1993; *Ziegler and Rasmussen*, 1998; *Ziegler et al.*, 2007], but according to our knowledge, no earlier study has shown closely matched direct comparisons between model simulation and observations.

[49] In addition, the observations show a low-level jet with wind speeds greater than 15 m s^{-1} about 100 km from the dryline on the moist side (Figure 14a), while the model predicts a similar jet structure with winds exceeding 20 m s^{-1} (Figure 14c). The western edge of this jet coincides with the eastern moisture band discussed later (cf. Figures 9c and 17), but because it is not directly responsible for the formation of the moisture band (as will be shown later) and its location is east of CI-C, it is believed that the jet does not play a direct role in determining the CI locations.

5.2.3. Vertical Structures Near CI-C

[50] The cross section through CI-C at 1800 (Figure 10e) is not too different from the corresponding one through CI-B (Figure 10c), except that the southeasterly flow component is stronger and extends further north as it overrides the northwesterly flow component behind the cold front (Figure 10e). Over the next 4 h or so, the cold front advanced by about 100 km (Figure 9) and by 2210, the initiation time of CI-C (Figure 9d and Figure 10f), with the secondary and primary cold fronts merged, the cold and moist air is now wedged underneath the warmer air coming from the southeast. In Figure 10f, the strongest vertical forcing is located near the leading edge of the cold air, or at the surface cold front. That is also where the 333 K θ_e contour is most elevated, and a deep column of cloud extends from the 2 km level up to the tropopause, corresponding to CI-C. The story with the dry run (Figure 11e) for CI-C is very similar to the earlier cases and therefore does not require further elaboration. For the no-heat-flux case, the θ_e and q_v structures for the CI-C case (Figure 11f) are closer to the cases with surface heating (Figure 10f and Figure 11e) than in earlier situations, which is reasonable because surface heating plays a smaller role in cold front than dryline cases. Still, with surface heating turned off, the CI at C is delayed to 2230, and cells remain weak and by 0000 they are mostly gone (not shown). This says that surface heating is still important for providing CAPE to sustain convection, even though cold frontal lifting is sufficient to lift the parcels to their initial LFC.

[51] The evolution of soundings located at C is generally similar to that at B (Figures 12e and 12f), except for generally more moist lower levels, a stronger cap and a larger CAPE at the beginning (Figure 12e). The BL moisture reaches 14–17 g kg^{-1} at the later times, with a saturated layer forming between 500 and 700 hPa by 2210 (Figure 12f) while some CIN still exists. In this case, the persistent lifting of moisture by the cold frontal interface should be primarily responsible for removing the strong cap in the 800–700 hPa layer and for bringing about saturation in the layer above 720 hPa (Figure 12f). This saturation layer matches the mid-level cloud in Figure 10f.

[52] The soundings at all three initiation locations have some commonalities. In all three cases, the moisture at the surface does not change much in the hours preceding the initiation, while the moisture in upper BL increases significantly to reach a state of nearly constant mixing ratio below the elevated BL top. The change in the surface temperature is not large, with the biggest change being in the deepening of a nearly neutrally stable BL. This BL eventually becomes deep enough so that the LCL and LFC are reached by the well mixed BL air and then moist convection occurs. Consequently, the vertical lifting in the dryline and/or cold frontal zone due to low-level convergence plays a very important role in this process while ample moisture supply is also necessary to ensure significant CAPE and to feed the elevated moisture bulge and later deep, moist convection. These are environmental ingredients necessary for deep moist convection [*Johns and Doswell*, 1992]. While such general processes are common for the three initiation regions, the exact process by which the lifting is realized is very different.

5.3. Mesoscale Moisture Bands and Their Roles in CI

[53] Noticeable features in the low level moisture fields are the two north-south-oriented moisture bands, as shown in Figure 9c and Figure 9d. These moisture bands (donated MB1 and MB2 in Figure 9c) contain q_v values exceeding 15 g kg^{-1} at 2138 and later times; they are located within the southerly moist flow east of the dryline and are spaced over 100 km apart. Some sign of MB1 is already evident at 1950 (Figure 9b) further south and the bands appear to extend northward with time and intercept the dryline and cold front, respectively (Figure 9d). Interestingly, the intercepting points appear to coincide with locations of CI-B and CI-C (Figures 9c and 9d). Important questions one would ask include: what role do these moisture bands play in the initiation of the two groups of convection there, if any? What caused the bands to form in the model? Did the bands form due to local moisture supply or due to moisture advection from the south? We try to answer these questions next.

5.3.1. The Western Moisture Band MB1

[54] We first examine the band near CI-B. To determine the source of the air parcels feeding the initial cell of CI-B, we initialize a parcel trajectory at the time and location of CI-B at the level of the updraft core, as denoted by the red dot in Figure 15f. This trajectory is then traced forward and backward in time and space, using model output at 1-min intervals. The projection of the trajectory onto the horizontal plane is plotted in Figures 15a, 15b, and 15c, together with the horizontal cross sections of wind and moisture fields at the level of the air parcel at the particular time of the plots. In Figures 15a, 15b, and 15c, the parcel location at the time of cross section is marked by a large red dot while small red dots are plotted every 10 min along the trajectory. East-west vertical cross sections through the parcel locations are plotted in Figures 15d, 15e, and 15f. It can be seen that from 1930 to 2138 (Figures 15a and 15c), the parcel moved northward by about 80 km, and rose from about 200 m AGL ($\sim$1.2 km MSL) at 1930 (Figure 15d) to 1.9 km MSL at 2030 then further up to about 6 km MSL at 2138. Most of the ascent occurred close to 2138 when the parcel became positively buoyant after LFC is reached. After the parcel rises to the upper levels, the trajectory turns east-northeastward due to the change in the prevailing wind direction (see Figure 15d for the winds at the $\sim$5.9 km MSL).

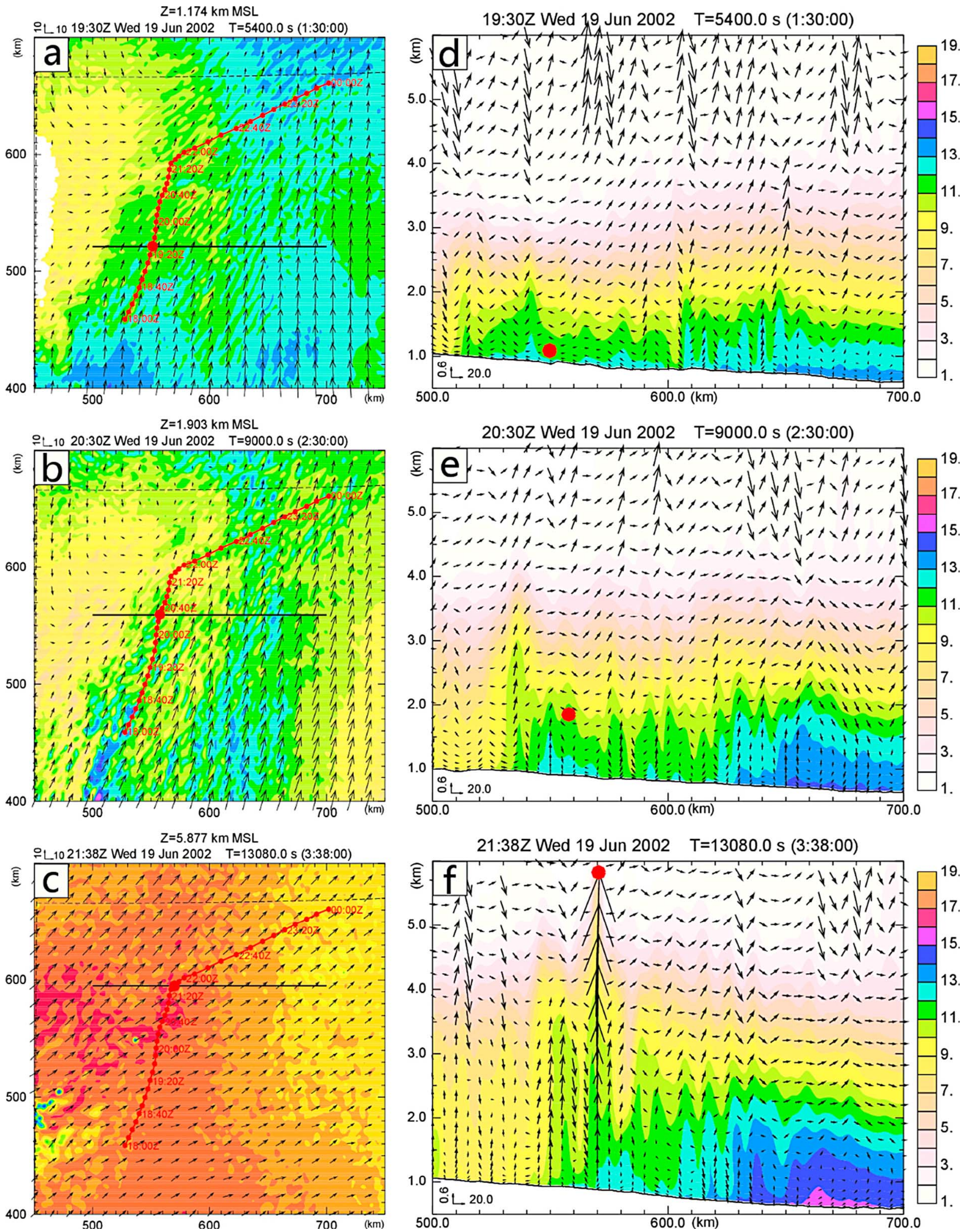

Figure 15. (a, b and c) Horizontal and (d, e and f) vertical cross sections of q_v (shaded, g kg^{-1}) and wind vector fields (m s^{-1}), at 1930 (Figures 15a and 15d), 2030 (Figures 15b and 15e), and 2138 (Figures 15c and 15f) UTC 19 June 2002. An air parcel trajectory was initialized at 2138 UTC, at the location of initial updraft core of CI-B. The position of this parcel at the three different times are marked by the large red dot in the plots, while the horizontal and vertical cross sections are plotted at the level and north-south location of the parcel at the times of the cross sections. In the horizontal sections, small dots show the parcel locations every 10 minutes, with their times leveled every 40 minutes. Note the different color scale used in Figure 15c for moisture.

[55] At 1930, the parcel that feeds the initial updraft core is traced back to y ≈ 520 km and ∼200 m AGL. This location appears to be at the leading edge of a developing moisture band at this time, given the >13 g kg^{-1} q_v values further south. The q_v values east and west of the parcel is slightly lower (Figure 15a). In the east-west vertical cross section through the parcel location (Figure 15d), a localized region of higher q_v (light blue color for q_v > 12 g kg^{-1}) is identifiable at the low level with its maximum located less than 10 km west of the parcel trajectory. Above the surface q_v maximum is a narrow upward extruding moisture bulge. Over the next hour, the cross-sectional area of q_v > 12 g kg^{-1} near the surface is enlarged and the moisture bulge becomes wider and deeper and more closely collocated with the parcel that has risen to 1.9 km MSL (Figure 15e). The near-surface enhanced moisture zone corresponds to moisture band MB1 in Figure 9. Within this region, underneath the air parcel, wind vectors are generally upward (Figure 15e), causing the parcel to rise as it moves northward. Therefore, even though moisture band structure is not readily visible at the level of air parcel in Figure 15b, the connection of the parcel with the low-level moisture band, the overlying moisture bulge, and the generally ascending motion is evident.

[56] Over the next hour or so, the northward moving air parcel eventually encountered the dryline, entering the region of much enhanced low-level convergence near the dryline-cold front triple point, and rises above LFC at the maximum moisture bulge, as discussed earlier, thereby causing the first cell initiation with CI-B (Figure 15f).

[57] From the vertical cross sections in Figure 15, we also see that the overall moist BL deepens as we follow the air parcel north (and more importantly as the time goes), with the BL top rising from an average of about 2.5 km MSL at 1930 based on the 6 g kg^{-1} contour, to above 3 km MSL at 2030, and to above 4 km MSL at 2138. The deepening of the western portion (west of x = 600 km) is more dramatic than the eastern portion at the later times, mostly due to its proximity to the dryline and associated convergence forcing. The general deepening of the BL is due to surface heating (the deepening happened at all three locations, not shown, and cf. the run with surface heat flux turned off), plus additional convergence lifting as the southerly flows approach the dryline or cold front to the north (cf. Figure 9).

5.3.2. The Eastern Moisture Band MB2

[58] Figure 9 shows that MB2 extends all the way to intercept with the cold front at 2210. In Figure 16, the eastern moisture band is most clearly visible in Figure 16b and Figure 16d; this has to do with the elevation of the horizontal cross section, and the timing. In general, the moisture band is more visible at the lower levels and more developed at the later times. For the northern cross-sections in Figure 16e and Figure 16f, MB2 becomes closer to the even stronger moisture band behind the cold front, making it hard to identify. At 2210, the designated time of CI-C, the parcel is about 5 km MSL, at the core of a well-developed initial cell. Over the 1 h 40 min proceeding this time, the parcel traveled by about 50 km (Figure 16c and Figure 16a), less than in the case of CI-B in a similar amount of the time. At 2030, the parcel is at about 1.3 km MSL (Figures 16a and 16d), located above surface q_v maximum (Figure 16d), although at this time MB2 is not yet fully developed (cf. Figure 9). Below the parcel is also generally rising motion. As the parcel moves northward, the moist BL deepens and the parcel rises to 1.9 km MSL (Figure 16e). Much more rapid ascent occurred shortly before 2210 as the parcel reaches the cold front convergence zone, carrying a somewhat higher level of moisture from the moisture band. Therefore, as in the earlier case, the initiation at the CI-C point appears to be helped by the fact that the parcel originated from a region where low-level moisture is higher than its surroundings.

5.3.3. Causes of Moisture Bands

[59] The cause of the moisture bands requires some investigation. One possibility is differential advection of high moisture from the south, but these bands do not appear to be associated with any southerly jet; the air parcels do not travel far enough either during the time period when the moisture bands form. To help determine the role of surface moisture flux, we re-run the simulation with the surface moisture flux turned off.

[60] Figure 17 shows the moisture and wind fields near the surface (at model level 5 about 300 m AGL) together with parcel trajectories initialized at the cross section within the two bands at 2210 UTC 19 June 2002, for the control, moisture-flux-off and heat-flux-off experiments. Figure 18 shows the corresponding fields in an east-west cross section cutting through the two moisture bands. The trajectories are included just to indicate how fast the air parcels move. By this time, the two moisture bands are even better developed in control experiment. The moisture bands in the moisture-flux-off experiment are still identifiable but are much weaker in terms of both cross-band moisture gradient and maximum moisture value. The bands in the heat-flux-off experiment have higher moisture values especially with the western band but the cross-band gradient is weaker and the gap between the bands is less well defined.

[61] Figure 18a shows that both bands are associated with an upward moisture bulge within the BL, and the bands are not associated with any southerly wind speed maximum or jet. The bands do appear to be located where the east-west gradient of the north-south wind speed is large. Figure 18d shows that there is enhanced east-west gradient of the u velocity component at the western edge of both moisture bands, due to the downward dip of westerly moment west of the bulge and the presence of easterly winds at the surface underneath the bulge. Such a wind pattern obviously creates surface wind convergence that would push the BL air upward and create the moisture bulge. The wind fields shown in Figure 18a suggest the presence of upward motion in the bulge region.

[62] The wind fields of the moisture-flux-off case are very similar to those of control (Figure 18b and Figure 18e). The associated moisture bulges are identifiable but much weaker; this should be because overall the BL moisture level is several g kg^{-1} lower. The fields with the heat-flux-off case are quite different (Figure 18c). Because of the lack of surface heating, the BL mixing is clearly much weaker or absent. As a result, there is accumulation of moisture near the surface provided by the moisture flux, giving rise to larger surface moisture values. Upward moisture bulges at the location of the two bands are still evident but much weaker; the east-west moisture gradient is much weaker than

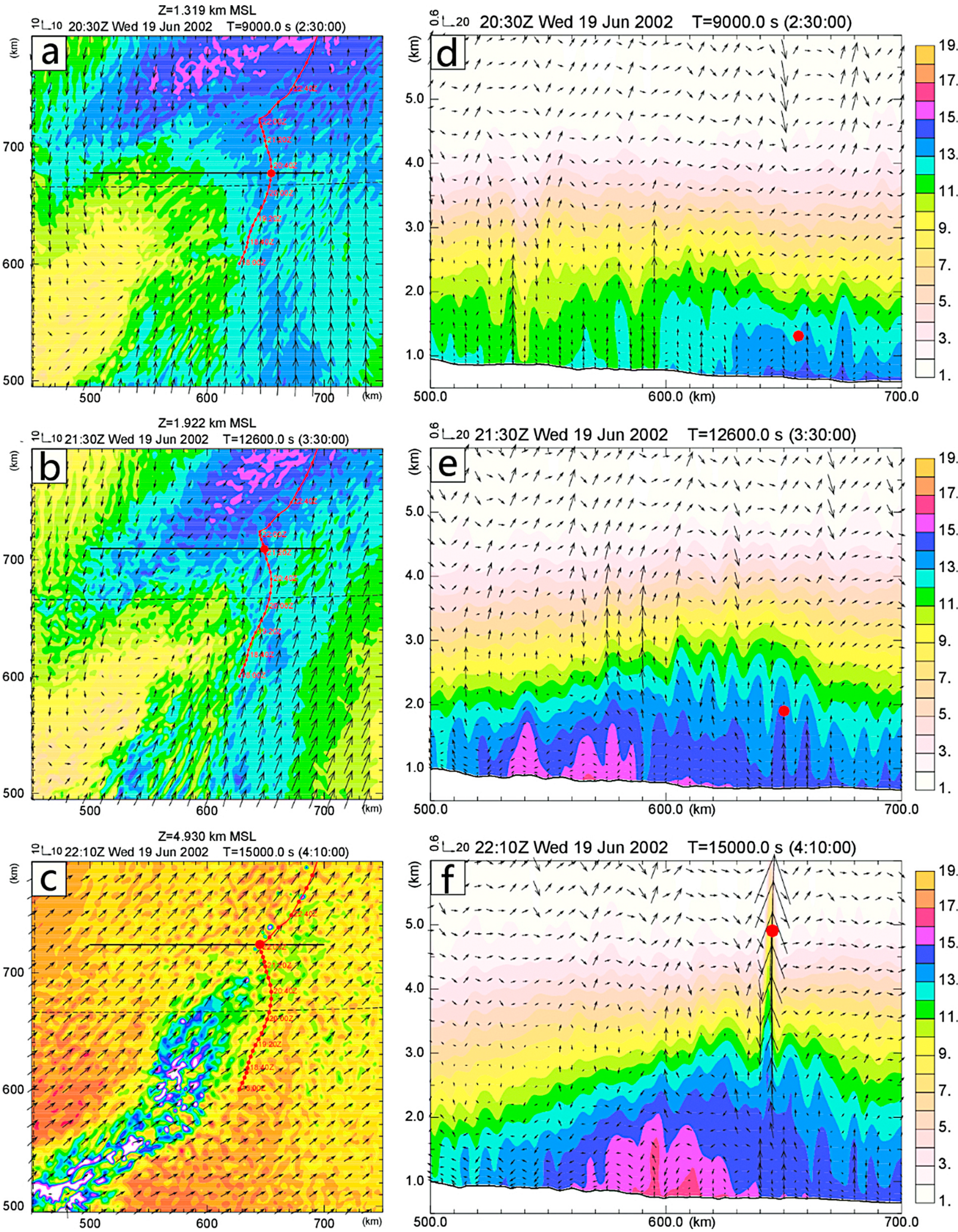

Figure 16. The same as Figure 15, but for air parcel trajectory initialized at 2210 UTC at the location of initial updraft core of CI-C. The times are (a and d) 2030, (b and e) 2130, and (c and f) 2210 UTC 19 June 2002.

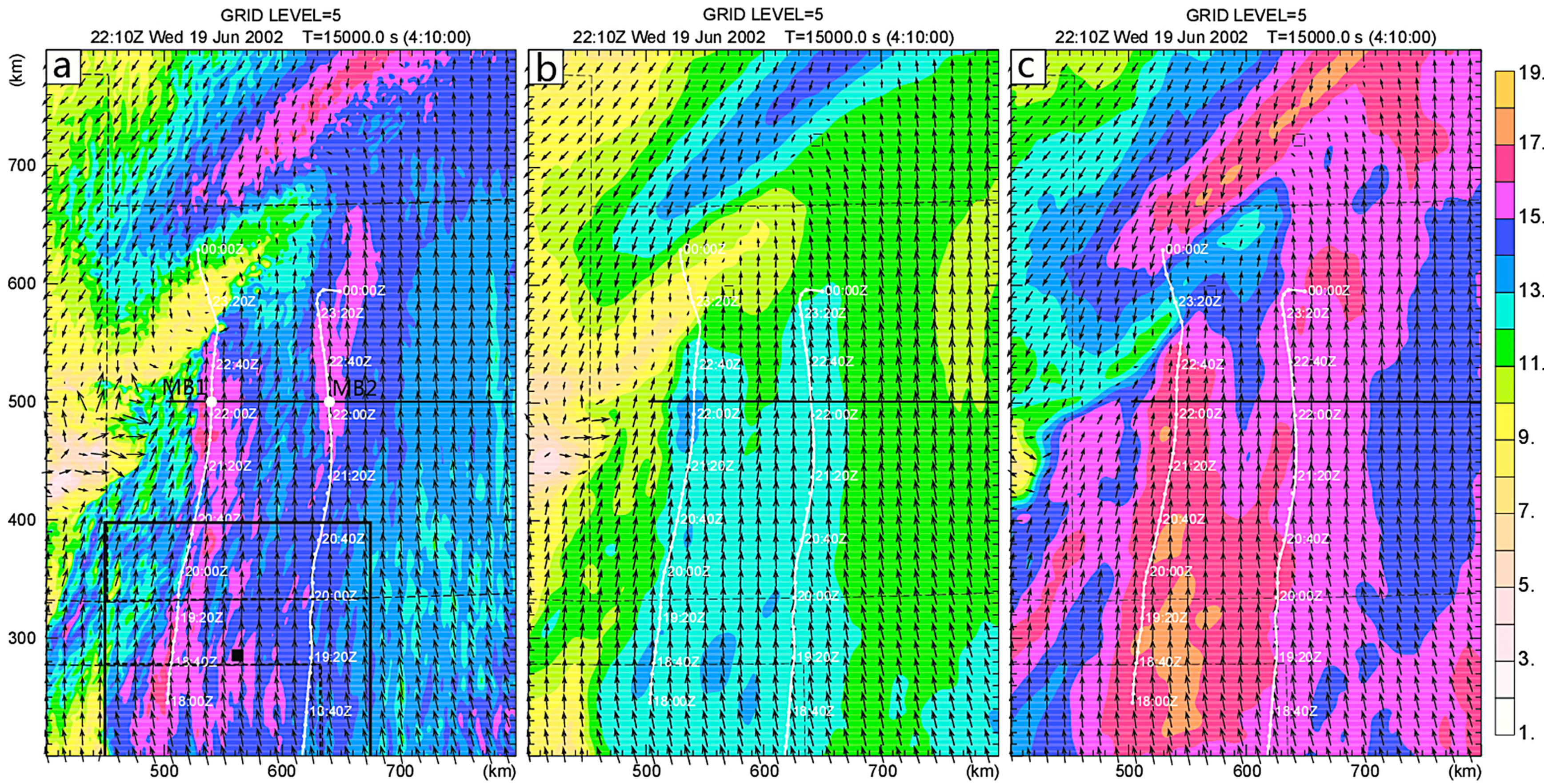

Figure 17. Water vapor mixing ratio q_v (shaded, g kg^{-1}) and wind vectors (m s^{-1}) at 2210 UTC 19 June 2002 at model level 5 or about 300 m AGL for (a) the control experiment, (b) experiment with surface moisture flux turned off, and (c) experiment with surface heat flux turned off. Trajectories shown were initialized at the points marked as MB1 and MB2, respectively. The box over Oklahoma panhandle in Figure 17a denotes a partial region of NCAR S-pol radar reflectivity observations shown in Figure 19 and the black square inside the box is the site of the radar.

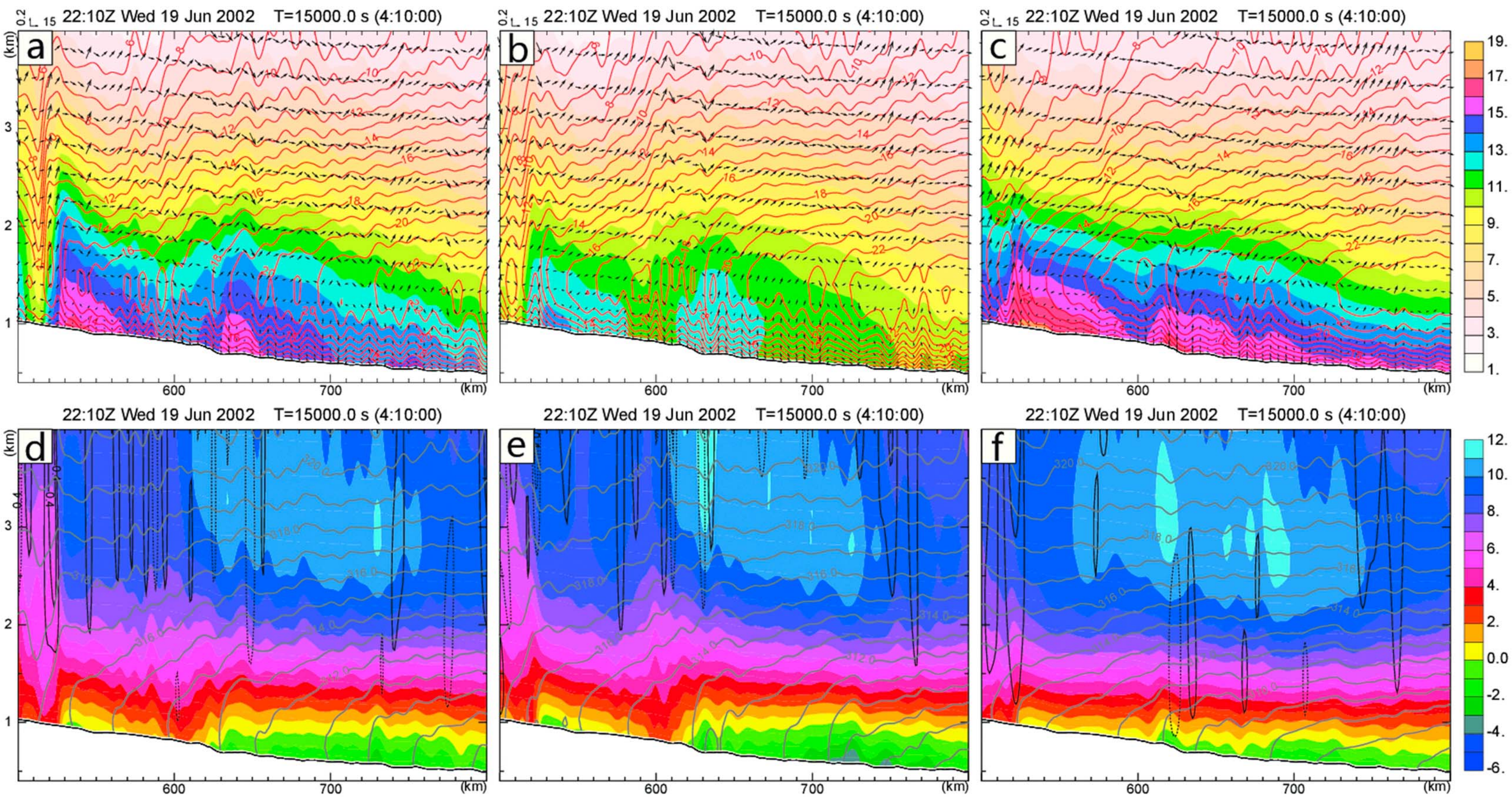

Figure 18. (a, b and c) The same as Figure 17 but for vertical cross sections of water vapor mixing ratio q_v (shaded, g kg^{-1}), southerly wind (contours, m s^{-1}), and wind vectors (m s^{-1}) through the corresponding lines in Figure 17. (d, e and f) The same as Figures 18a–18c but for the east-west wind component (shaded, m s^{-1}), vertical velocity (black solid and dashed contours, m s^{-1}), and potential temperature (gray solid contours, K).

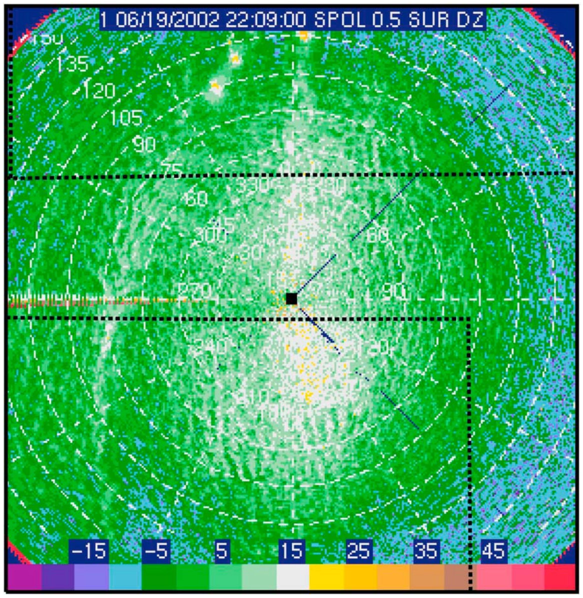

Figure 19. NCAR S-pol radar reflectivity at 0.5° elevation at 2209 UTC, June 19, 2002. The radar was located at (36.57N, 100.78W).

control. Even more different is with the *u* velocity component (Figure 18f); the east-west gradient of *u* velocity at the surface is much weaker and no easterly wind is found underneath the western bulge. Downward dip of westerly wind west of the eastern bulge is not absent. All of these suggest that the surface heating plays an important role in the establishment of the two moisture bands and the associated BL structures. In fact, the vertical structures we are observing suggest that the moisture bands form due to very similar processes that enhance daytime dryline on the slope terrain and sometimes cause the dryline to move eastward. For this reason, the western edges of the moisture bands, as well as the primary dryline further to the west can be considered "multiple drylines," analogous to the "double drylines" that have been identified in a number of studies [e.g., *Crawford and Bluestein*, 1997; *Hane et al.*, 1993; *Weiss et al.*, 2006].

[63] A conceptual model on the effects of sloping terrain on the development and movement of drylines can be found in *Bluestein* [1993] which is consistent with the modeling study of *Sun and Wu* [1992]. With this model, heating over the elevated terrain further west would create more vertical mixing that would bring westerly momentum and drier air down toward the surface and enhance east-west wind convergence there. This is clearly seen in Figure 18a and Figure 18d west of the moisture bands but is weaker in Figure 18c and Figure 18f when surface heating is turned off. Underneath the moisture bulges, easterly flows are seen to develop which further enhance the convergence. Such "indirect dryline circulations" have been documented in observational data [*Weiss et al.*, 2006], and *Sun and Wu* [1992] referred to them as "inland sea breeze circulations" due to the differential heating along the sloping surface. As a result of such differential heating, potential temperature in the BL increases toward west, a situation that would promote sinusoidal circulation with easterly winds at the surface. The surface easterly flows are interrupted where enhanced downward mixing of westerly moment occurs. The enhanced vertical mixing west of the moisture bands and enhanced vertical circulation at the location of moisture bulges/bands also explain the structure of the north-south wind component in the cross section (Figure 18a).

[64] In the experiment where the surface moisture flux is turned off, similar processes also occur, giving rise to similar wind and temperature structures (Figure 18b and (Figure 18e) but the moisture content in the BL is much lower, therefore the moisture bands are much weaker (Figure 18b and Figure 17b). We note that without surface moisture flux, CI in B region is delayed until 2230 and cells remain weak and last for less than one hour while CI in C region never occurs. The effect on CI-A is similar as turning off surface heat flux (not shown).

[65] *Sun and Wu* [1992] found that soil moisture gradient also had effect on the dryline moisture gradient, so did more recent studies such as *Grasso* [2000]. We noticed presence of soil moisture inhomogeneity in our initial condition but an experiment in which the initial volumetric soil moisture was set to a constant of 0.2 m^3 m^{-3} produced very similar moisture bands and associated structures (not shown); therefore soil moisture inhomogeneity is not the primary cause of the moisture bands. Given that the moisture bands are associated with enhanced surface convergence near their western edge and with enhanced upward motion and moisture bulge, it is even less surprising that their intercepting points with the primary dryline or cold front provide preferred locations for CI. Finally, as evidence that the model simulated moisture bands and associated convergence zones may indeed be real on that day, we show in Figure 19 the 0.5° elevation reflectivity observation by the NCAR S-Pol radar deployed in the Oklahoma Panhandle area, at the time of the fields in Figure 17. A north-south band of enhanced reflectivity indicating enhanced vertical motion with higher concentration of scatters (mostly bugs) can be seen passing through the radar site and this feature is stronger between 2000 and 2200 in the radar data. There is another narrow band further west roughly 75 km from the radar site. We believe these reflectivity bands roughly correspond to the moisture bands found in the model (comparing Figure 19 with boxed region in Figure 9d and Figure 17a). These bands are hard to identify in regular surface observations due to their coarse resolution [*Weiss et al.*, 2006].

6. Summary and Conclusions

[66] In this study, the 19 June 2002 convective initiation (CI) case from IHOP_2002 is simulated using the ARPS model. The initial condition is provided by a high-resolution analysis of the ARPS 3DVAR that contains routine as well as special upper-air and surface observations collected during IHOP. A 1000 $\times$ 1000 km^2 grid with a 1-km grid spacing nested inside a larger 3-km grid is able to resolve important mesoscale circulations as well as individual cells of deep moist convection.

[67] The model-simulated three groups of cells are realistic. The first group of convection, denoted CI-A, started along a dryline near the southeast corner of Colorado. The second group, CI-B, formed along the dryline over northwest Kansas close to a dryline-cold front triple point, while

the third group, CI-C, was located further north along the cold front over south-central Nebraska (Figures 3 and 5). The initiation of an initial cell close to the location of observed cell group A is predicted about 5 km west of the observed location with a $\sim$20 min delay, while the timings of predicted CI-B and CI-C are accurate to within 30 min in time and $\sim$50 and 60 km in space. The general evolution of the three predicted CIs also verifies reasonably well against radar observations. The model-simulated three groups of cell are realistic enough to allow for a detailed analysis on the mesoscale environment and evolution that lead to the cell initiations at the three locations.

[68] Among the three CIs, CI-A is most typical of dryline initiation. Vertical cross sections through the initiation location show typical dryline structures with an upward moisture bulge forced by lifting above the surface dryline convergence zone. For CI-B, the model predicted mesoscale structures agree with available aircraft dropsonde observations very well. Strong low-level convergence resulting from opposing cold front and dryline circulations produced deep symmetric upwelling of moist air, and the convection is initiated where the vertical lifting is strongest and the moisture supply is further enhanced by a BL moisture band intercepting the dryline. The initiation at location C is more typical of frontal convection where warm moist air rides over the frontal surface while deep convection is first initiated at the front edge of the cold air where moisture supply is ample. A moisture band feeding the initiation location is also evident with CI-C. Analyses show that the moisture bands form due to similar processes that create and enhance surface moisture gradient at a dryline over a sloping terrain and such processes appear to have created "multiple drylines" (with the secondary ones at the western edges of the moisture bands within the moist air) on this day. Evidence of such moisture bands is found in the S-pol reflectivity data. The fact that these moisture bands are associated with enhanced vertical motion and upward moisture bulges makes their intercepting points with the primary dryline and the cold front even more favorable for CI.

[69] Vertical cross sections and extracted soundings at the locations of CI show that the establishment of a deep well-mixed moist BL is common in the hours leading to CI while low-level convergence provides the primary forcing for the establishment of upward moisture bulge at the dryline or cold front. Convective cells are found to first form at the crest of the moisture bulges and the parcels that feed the convective updrafts are rooted from the moist/warm side of dryline/cold front.

[70] The above conclusions are supported by additional sensitivity experiments in which the condensation process, surface heat flux, or surface moisture flux is turned off, respectively, and by tracing air parcels in the initial updraft cores backward in time along time-dependent trajectories. When surface moisture flux is turned off in the model, CI-A (which occurs earlier in the model run and is therefore affected less by surface moisture flux) still occurs but the subsequent convection is much weaker. CI-B is delayed by about 30 min and the convection remains weak and dissipates after 1 h. CI-C never occurs. When the surface heat flux is turned off, the effects on the CIs are similar as turning off moisture flux, except that CI-C still occurs but the convection dissipates within 1.5 h. Apart from helping us understand the initiation processes, these results also indicate large sensitivity of CI and subsequent convection evolution to surface moisture and temperature fluxes.

[71] The agreement with observations of the model simulated temperature, moisture and wind structures in a cross section sampled by dropsonde data represents one of the first such close comparisons in a similar context, and the close agreement indicates physical realism of the model simulation, and demonstrates the abilities of a modern nonhydrostatic numerical model with the help of high-resolution observations. The model simulation starting from the operational 1800 UTC Eta model analysis was not as good (not shown).

[72] **Acknowledgment.** This work was primarily supported by NSF grants AGS-0530814 and AGS-0802888. Qiwei Wang was also supported by the CNSF under grant 40705019 and partially supported by grants GYHY200706033 and GYHY201006004 from the Special Public Sector Research of China. M. Xue was also supported by NSF grants AGS-0608168, AGS-0750790, AGS-0941491, and OCI-0905040. Assistance with initial data preparation was provided by Keith Brewster. The first author appreciates helps from Yunheng Wang, Fanyou Kong, Jidong Gao and Guoqing Ge with the use of the ARPS system. Discussions with David Schultz significantly improved the manuscript. Supercomputers operated by TACC of University of Texas and by OSCER of University of Oklahoma were used for the computations. Revisions to the paper were completed during M. Xue's visit at Nanjing University, supported by the 'Thousand Person Plan' of China. We thank Tammy Weckwerth and two anonymous reviewers, whose comments improved the manuscript.

References

Bluestein, H. B. (1993), *Synoptic-Dynamic Meteorology in Midlatitudes*, vol. 2, *Observations and Theory of Weather Systems*, 594 pp., Oxford Univ. Press, New York.

Chou, M.-D. (1990), Parameterizations for the absorption of solar radiation by O_2 and CO_2 with application to climate studies, *J. Clim.*, *3*, 209–217, doi:10.1175/1520-0442(1990)003<0209:PFTAOS>2.0.CO;2.

Chou, M.-D. (1992), A solar radiation model for use in climate studies, *J. Atmos. Sci.*, *49*, 762–772, doi:10.1175/1520-0469(1992)049<0762:ASRMFU>2.0.CO;2.

Chou, M.-D., and M. J. Suarez (1994), An efficient thermal infrared radiation parameterization for use in general circulation models, *NASA Tech. Memo.*, *104606*, 85 pp.

Crawford, T. M., and H. B. Bluestein (1997), Characteristics of dryline passage during COPS-91, *Mon. Weather Rev.*, *125*, 463–477, doi:10.1175/1520-0493(1997)125<0463:CODPDC>2.0.CO;2.

Crook, N. A. (1996), Sensitivity of moist convection forced by boundary layer processes to low-level thermodynamic fields, *Mon. Weather Rev.*, *124*, 1767–1785, doi:10.1175/1520-0493(1996)124<1767:SOMCFB>2.0.CO;2.

Fritsch, J. M., and R. E. Carbone (2004), Improving quantitative precipitation forecasts in the warm season: A USWRP research and development strategy, *Bull. Am. Meteorol. Soc.*, *85*, 955–965, doi:10.1175/BAMS-85-7-955.

Gao, J.-D., M. Xue, K. Brewster, and K. K. Droegemeier (2004), A three-dimensional variational data analysis method with recursive filter for Doppler radars, *J. Atmos. Oceanic Technol.*, *21*, 457–469, doi:10.1175/1520-0426(2004)021<0457:ATVDAM>2.0.CO;2.

Grasso, L. D. (2000), A numerical simulation of dryline sensitivity to soil moisture, *Mon. Weather Rev.*, *128*, 2816–2834, doi:10.1175/1520-0493(2000)128<2816:ANSODS>2.0.CO;2.

Hane, C. E., C. L. Ziegler, and H. B. Bluestein (1993), Investigation of the dryline and convective storms initiated along the dryline: Field experiments during COPS-91, *Bull. Am. Meteorol. Soc.*, *74*, 2133–2145, doi:10.1175/1520-0477(1993)074<2133:IOTDAC>2.0.CO;2.

Hu, M., M. Xue, J. Gao, and K. Brewster (2006), 3DVAR and cloud analysis with WSR-88D level-II data for the prediction of Fort Worth tornadic thunderstorms. Part II: Impact of radial velocity analysis via 3DVAR, *Mon. Weather Rev.*, *134*, 699–721, doi:10.1175/MWR3093.1.

Jankov, I., W. A. Gallus, M. Segal, and S. E. Koch (2007), Influence of initial conditions on the WRF–ARW model QPF response to physical parameterization changes, *Weather Forecast.*, *22*, 501–519, doi:10.1175/WAF998.1.

Johns, R. H., and C. A. Doswell III (1992), Severe local storm forecasting, *Weather Forecast.*, *7*, 588–612, doi:10.1175/1520-0434(1992)007<0588:SLSF>2.0.CO;2.

Lin, Y.-L., R. D. Farley, and H. D. Orville (1983), Bulk parameterization of the snow field in a cloud model, *J. Clim. Appl. Meteorol.*, *22*, 1065–1092, doi:10.1175/1520-0450(1983)022<1065:BPOTSF>2.0.CO;2.

Liu, H., and M. Xue (2008), Prediction of convective initiation and storm evolution on 12 June 2002 during IHOP. Part I: Control simulation and sensitivity experiments, *Mon. Weather Rev.*, *136*, 2261–2282, doi:10.1175/2007MWR2161.1.

Markowski, P., C. Hannon, and E. Rasmussen (2006), Observations of convection initiation “failure” from the 12 June 2002 IHOP deployment, *Mon. Weather Rev.*, *134*, 375–405, doi:10.1175/MWR3059.1.

Marquis, J. N., Y. P. Richardson, and J. M. Wurman (2007), Kinematic observations of misocyclones along boundaries during IHOP, *Mon. Weather Rev.*, *135*, 1749–1768, doi:10.1175/MWR3367.1.

Miao, Q., and B. Geerts (2007), Finescale vertical structure and dynamics of some dryline boundaries observed in IHOP, *Mon. Weather Rev.*, *135*, 4161–4184, doi:10.1175/2007MWR1982.1.

Murphey, H. V., R. M. Wakimoto, C. Flamant, and D. E. Kingsmill (2006), Dryline on 19 June 2002 during IHOP. Part I: Airborne Doppler and LEANDRE II analyses of the thin line structure and convection initiation, *Mon. Weather Rev.*, *134*, 406–430, doi:10.1175/MWR3063.1.

Schaefer, J. T. (1974), The life cycle of the dryline, *J. Appl. Meteorol.*, *13*(4), 444–449, doi:10.1175/1520-0450(1974)013<0444:TLCOTD>2.0.CO;2.

Sipprell, B. D., and B. Geerts (2007), Finescale vertical structure and evolution of a preconvective dryline on 19 June 2002, *Mon. Weather Rev.*, *135*, 2111–2134, doi:10.1175/MWR3354.1.

Stano, G. (2003), A case study of convective initiation on 24 May 2002 during the IHOP field experiment, MS thesis, 106 pp., Univ. of Okla., Norman.

Sun, W.-Y., and C.-Z. Chang (1986), Diffusion model for a convective layer. Part I: Numerical simulation of convective boundary layer, *J. Appl. Meteorol.*, *25*, 1445–1453, doi:10.1175/1520-0450(1986)025<1445:DMFACL>2.0.CO;2.

Sun, W.-Y., and C.-C. Wu (1992), Formation and diurnal variation of the dryline, *J. Atmos. Sci.*, *49*, 1606–1619, doi:10.1175/1520-0469(1992)049<1606:FADVOT>2.0.CO;2.

Tong, M., and M. Xue (2005), Ensemble Kalman filter assimilation of Doppler radar data with a compressible nonhydrostatic model: OSS experiments, *Mon. Weather Rev.*, *133*, 1789–1807, doi:10.1175/MWR2898.1.

Trier, S. B., F. Chen, K. W. Manning, M. A. LeMone, and C. A. Davis (2008), Sensitivity of the PBL and precipitation in 12-day simulations of warm-season convection using different land surface models and soil wetness conditions, *Mon. Weather Rev.*, *136*, 2321–2343, doi:10.1175/2007MWR2289.1.

Wakimoto, R. M., and H. V. Murphey (2010), Analysis of convergence boundaries observed during IHOP_2002, *Mon. Weather Rev.*, *138*, 2737–2760, doi:10.1175/2010MWR3266.1.

Wakimoto, R. M., H. V. Murphey, R. G. Fovell, and W.-C. Lee (2004), Mantle echoes associated with deep convection: Observations and numerical simulations, *Mon. Weather Rev.*, *132*, 1701–1720, doi:10.1175/1520-0493(2004)132<1701:MEAWDC>2.0.CO;2.

Weckwerth, T. M., and D. B. Parsons (2006), A review of convection initiation and motivation for IHOP_2002, *Mon. Weather Rev.*, *134*, 5–22, doi:10.1175/MWR3067.1.

Weckwerth, T. M., J. W. Wilson, and R. M. Wakimoto (1996), Thermodynamic variability within the convective boundary layer due to horizontal convective rolls, *Mon. Weather Rev.*, *124*, 769–784, doi:10.1175/1520-0493(1996)124<0769:TVWTCB>2.0.CO;2.

Weckwerth, T. M., D. B. Parsons, S. E. Koch, J. A. Moore, M. A. LeMone, B. B. Demoz, C. Flamant, B. Geerts, J. Wang, and W. F. Feltz (2004), An overview of the international H_2O project (IHOP_2002) and some preliminary highlights, *Bull. Am. Meteorol. Soc.*, *85*, 253–277, doi:10.1175/BAMS-85-2-253.

Weiss, C. C., H. B. Bluestein, and A. L. Pazmany (2006), Finescale radar observations of the 22 May 2002 dryline during the International H_2O Project (IHOP), *Mon. Weather Rev.*, *134*, 273–293, doi:10.1175/MWR3068.1.

Wilson, J. W., and R. D. Roberts (2006), Summary of convective storm initiation and evolution during IHOP: Observational and modeling perspective, *Mon. Weather Rev.*, *134*, 23–47, doi:10.1175/MWR3069.1.

Xue, M., and W. J. Martin (2006a), A high-resolution modeling study of the 24 May 2002 case during IHOP. Part II: Horizontal convective rolls and convective initiation, *Mon. Weather Rev.*, *134*, 172–191, doi:10.1175/MWR3072.1.

Xue, M., and W. J. Martin (2006b), A high-resolution modeling study of the 24 May 2002 case during IHOP. Part I: Numerical simulation and general evolution of the dryline and convection, *Mon. Weather Rev.*, *134*, 149–171, doi:10.1175/MWR3071.1.

Xue, M., J. Zong, and K. K. Droegemeier (1996), Parameterization of PBL turbulence in a multi-scale non-hydrostatic model, paper presented at 11th AMS Conference on Numerical Weather Prediction, Am. Meteorol. Soc., Norfolk, Va.

Xue, M., K. K. Droegemeier, and V. Wong (2000), The Advanced Regional Prediction System (ARPS)—A multiscale nonhydrostatic atmospheric simulation and prediction tool. Part I: Model dynamics and verification, *Meteorol. Atmos. Phys.*, *75*, 161–193, doi:10.1007/s007030070003.

Xue, M., K. K. Droegemeier, V. Wong, A. Shapiro, K. Brewster, F. Carr, D. Weber, Y. Liu, and D.-H. Wang (2001), The Advanced Regional Prediction System (ARPS)—A multiscale nonhydrostatic atmospheric simulation and prediction tool. Part II: Model physics and applications, *Meteorol. Atmos. Phys.*, *76*, 143–165, doi:10.1007/s007030170027.

Xue, M., D.-H. Wang, J.-D. Gao, K. Brewster, and K. K. Droegemeier (2003), The Advanced Regional Prediction System (ARPS), storm-scale numerical weather prediction and data assimilation, *Meteorol. Atmos. Phys.*, *82*, 139–170, doi:10.1007/s00703-001-0595-6.

Ziegler, C. L., and C. E. Hane (1993), An observational study of the dryline, *Mon. Weather Rev.*, *121*, 1134–1151, doi:10.1175/1520-0493(1993)121<1134:AOSOTD>2.0.CO;2.

Ziegler, C. L., and E. N. Rasmussen (1998), The initiation of moist convection at the dryline: Forecasting issues from a case study perspective, *Weather Forecast.*, *13*, 1106–1131, doi:10.1175/1520-0434(1998)013<1106:TIOMCA>2.0.CO;2.

Ziegler, C. L., T. J. Lee, and R. A. Pielke Sr. (1997), Convective initiation at the dryline: A modeling study, *Mon. Weather Rev.*, *125*, 1001–1026, doi:10.1175/1520-0493(1997)125<1001:CIATDA>2.0.CO;2.

Ziegler, C. L., E. N. Rasmussen, M. S. Buban, Y. P. Richardson, L. J. Miller, and R. M. Rabin (2007), The “triple point” on 24 May 2002 during IHOP. Part II: Ground-radar and in-situ boundary layer analysis of cumulus development and convection initiation, *Mon. Weather Rev.*, *135*, 2443–2472, doi:10.1175/MWR3411.1.